Control of Oligonucleotide Conformation on Nanoparticle Surfaces for Nanoscale Heat Transfer Study

by

Sunho Park

B.S., Mechanical Engineering (1998)
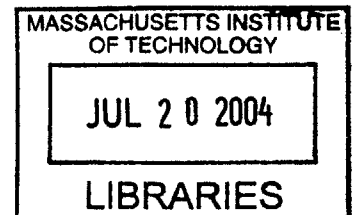
Seoul National University

Submitted to the Department of Mechanical Engineering
in Partial Fulfillment of the Requirements for the Degree of
Master of Science in Mechanical Engineering

at the

Massachusetts Institute of Technology

June 2004

Signature of Autuor.......

....
Department of Mechanical Engineering
May 7, 2004

Certified by....

....
Kimberly Hamad-Schifferli
Assistant Professor of Mechanical Engineering
Thesis Supervisor

Accepted by..........

....
Ain A. Sonin
Chairman, Department Committee on Graduate Students

Control of Oligonucleotide Conformation on Nanoparticle Surfaces for Nanoscale Heat Transfer Study

by

Sunho Park

Abstract

Metal nanoparticles can be used as antennae covalently linked to biomolecules. External alternating magnetic field can turn on and off the biological activity of the molecules due to induction heating from the particles that changes the temperature around the molecules. Here an experimental scheme towards direct temperature probing is proposed to predict the behavior of the antenna. Oligonucleotides modified with photosensitive molecules are conjugated with gold nanoparticles and report the temperature at their positions within some nanometers' distance from the particles. However, oligos have a known tendency to stick to gold surfaces. To locate the probes at desired position, 6-mercapto-1-hexanol (MCH) is used to reduce oligonucleotides' adsorption to the surface of gold. The experimental result shows that oligos on particle's surface can be stretched radially without any reduction of coverage ratio. Optimal MCH concentration and reaction time highly depend on the concentration of MCH and the conjugates as well as reaction time and the size of the molecules.

Thesis Supervisor: Kimberly Hamad-Schifferli
Title: Assistant Professor of Mechanical Engineering

Table of Contents

Chapter 1: Introduction

There has been enormous effort in developing "bottom up" manufacturing to replace traditional "top down" methods. However, these approaches have reached limitations. Nature provides many remarkable biomolecular machines that perform with great efficiency, precision, and accuracy. A goal is to come up with a means of controlling biomolecular activity to utilize Nature's engineering. The method of control should be precise and specific as well as compatible with the complex and highly disordered environments inside cells.

Metal nano-particles can be used as antennas to control the activity of biomolecules[1]. The antennas are heated by an external radio-frequency magnetic field, which generates eddy currents in the nanoparticles that create heat. The heat generated in the particle propagates to the DNA, protein, or enzyme covalently linked to the antenna. The biomolecule is thus denatured slightly, thereby changing its biological activity. Under the absence of the magnetic field, the heat is dissipated from the biomolecule, allowing it to renature, and recovers its activity rapidly. This has been used as a way to control activity of a biomolecule in a way that is both reversible and selective in solution. These properties are dependent on the heat localization around the nanoparticle. This will become a crucial issue if implemented in cells, where the environment is extremely crowded and not heating surrounding proteins will be difficult. Consequently, it is of central importance to characterize the heat transfer and heat localization around nanoparticles when heated by an alternating magnetic field. Once we can precisely predict the amount of heat generated in antenna and the temperature profile near the molecules, we can finely control activity.

However, heat transfer between antenna and biomolecule is expected to occur within only a few nanometers, where the physics of the heat carrier transport is inherently different from the macroscale and continuum approaches. Nanoscale heat transfer is not well understood theoretically, especially in the context of molecular systems. In addition, traditional methods for probing temperature are applicable only for macroscale systems. Consequently, the goal is to experimentally map the temperature profile around nanoparticles and also heating kinetics. The proposed approach is to utilize DNA molecules

since increased temperatures induce conformational changes in DNA. This can be monitored by optical absorption and fluorescence spectra of functionally modified DNA strands. By varying the length of DNA attached to the metal nanoparticle, we can map the actual temperature distribution for a given particle. This can be compared to calculations for heat transfer from nanoparticles. This requires control of conformation of oligos attached to nanoparticles, which makes it possible to control the real lengths of the oligos on the particles.

1.1 Previous research

There are many known techniques for conjugating metal clusters and biomolecules[2]. From the methods, multi-dimensional array of nanoscale metal pieces can be achieved by use of unique characteristics of biomolecules such as hybridization of complementary DNA strands[3,4].

Regarding with nanoparticles, there has been another big research area dealing with hyperthermia utilizing induction heating in ferromagnetic particles[5-7]. It is advantageous compared to global heating in that heating is localized in a very narrow area. Thus only target spots are thermally treated under magnetic field without damaging environment. A remarkable study that grafted hyperthermia phenomena for the first time onto the research on metal-biomolecule conjugates was recently reported. Its superiority is in the fact that biological behavior in nanoscale can be remotely controlled by external magnetic field. By changing the type of the metal particle, we can have different channels of control and this enables selective control of complex biological system. Figure 1.1 shows the possibility of remote controls. Under the presence of magnetic field, the gold particle is inductively heated and the hairpin-shaped oligos are released from its hybridized form. This can be detected by absorbance measurement at 260nm, a general method for quantifying the degree of DNA's hybridization-dehybridization. We can see that oligo's conformation is quickly responding to the external magnetic field (1GHz).

The research given in this paper is motivated by the above study. To utilize the ability of nanosize antenna it is essential to reveal its heat generation and heat propagation behavior. This paper suggests a method of direct temperature probing that works in the very

6

small size scale. Since conformational change of DNA on particle surface is very important for proper function of the probes, 6-mercapto-1-hexanol is introduced to modify the surface of the nanoparticle.
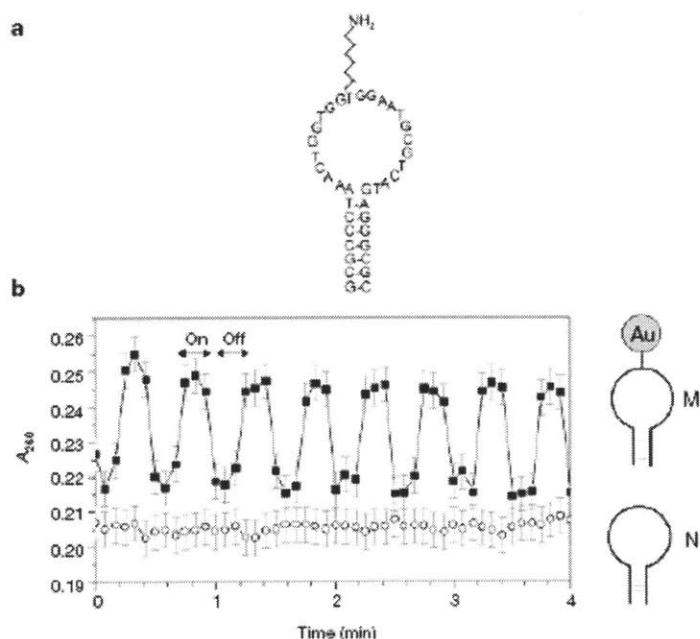
Figure 1.1 (a) Sequence of the self-complementary oligo for 7 bases. It has a primary amine group that is covalently linked to 1.4nm gold nanoparticle.
(b) Absorbance at 260nm of two solutions having oligos conjugated with the gold particle(M) and the same oligos without the gold particle(N), respectively. 1GHz magnetic field is used. Copied image[1].

1.2 Snapshot of the paper

Gold particle - DNA conjugate is mostly concerned throughout the paper. But some possible issues might arise to utilize the conjugate system quantitatively. How much is the actual power generation? What parameters will control the heating? How does the size effect change the heat transfer mechanism? How does the DNA look like around the particle? and how can we control its behavior based on the answers from the questions? Here is a part of the answers suggested, though there is a lot of space to be filled through further research.

The main topic of chapter 2 is heat generation and propagation in nano-size system. We will discuss how alternating magnetic field induces power dissipation in metal clusters. Some classical formulas are introduced and recently developed equations considering size effect also are mentioned. By literature review, we will see the availability of classical heat transfer equations on nano-scale heat propagation. A sample calculation of Au particle - water system will be given.

In chapter 3, an experiment on direct temperature probing is proposed. Fluorescence modified DNA's are conjugated with gold particles and its conformation change will give the information on temperature. Root-mean-square end-to-end length of the conjugates is closely related with the distance from particle center to the probing position. We will discuss some theories on polymer chain and its conformation of which the most important parameter is its persistence length.

Surface modification experiment on gold-DNA conjugate is given in chapter 4. 6-mercapto-1-hexanol prevents DNA adsorbing on the gold particle's surface and improve hybridization ability of the linked DNA. To analyze the conformational change of DNA, Ferguson plot method is used. A short review on the method will be given.
Chapter 5 briefly shows the summary of the research given in chapter 2~4 followed by some possible future work.

Chapter 2: Heating Mechanism of nanoparticle-biomolecule system

The keys of the function of Au particle antenna are heat generating and heat propagation. Temperature around biomolecules strongly affects the molecules' activity, so we need to get an exact picture of temperature profile. The temperature profile itself depends on the heat flux from the particle. Difficulties arise from Au particle - biomolecules syetem are mainly related with the size scale. It is now very well known that nanostructure is affected by quantum or classical size effect. The former is from the energy band structure. Bulk material has almost continuous energy level, whereas nanostructure has limited number of energy levels that give wider gap between the bands. The latter tells about transport phenomena of carriers. In the macrosystem, detail movements of carriers are generally ignored by being averaged, but if the length scale of structure becomes comparable with that of carriers' movement, we need to directly deal with the carriers' microscopic behavior.

In this chapter, heat generating and heat transfer mechanisms are explained especially for 10nm Au particle and oligo system, which is used for the oligo conformation control experiment in chapter 4 and future work. Ch. 2.1 deals with some heat generation mechanisms and ch.2.2 is describing heat propagation phenomena. Application to our system is given in ch.2.2, too.

2.1 Heat generating mechanisms in nanoparticle
2.1.1 Introduction

There are some heating mechanisms originated from electromagnetic wave (or magnetic wave) incident on metal substance. One method is induction heating, commonly used in industries. Due to high electrical conductivity, we have to apply very high current if we want direct Joule heating of metal. We may put the object in a hot chambers or make it contact with heat source at high temperature, but still there is a certain time scale for sufficient heating. So induction heating gives similar convenience as microwave ovens do, though their mechanisms are fundamentally different. There are also other heating processes such as Neel relaxation, Brownian relaxation and hysterisis loss. They mainly

occur for magnetic particles. Our primary concern is how the heating mechanisms look like for nanoparticle-magnetic field system. It has not been clearly shown that how the size effect play a role in the mechanisms, but we are still able to infer some physical sense from classical approach to the phenomena.

2.1.2 Joule heating

From Maxwell equations, equation 2.1 is derived with a constitutive law (equation 2.2) [8]

$$\frac{1}{\mu \sigma_e} \nabla^2 H = \frac{\partial H}{\partial t} \tag{2.1}$$

$$B = \mu H \tag{2.2}$$

We can solve equation 2.1 for the particle to find the distribution of magnetic field. From the distribution, we can get current density (eddy current) by Ampere's law. The time-averaged power is calculated by equation 2.3 with eddy current.

$$\langle P \rangle = \frac{1}{2} \text{Re} \left\{ \int \left(E \cdot J^* \right) dV \right\} \tag{2.3}$$

Induction heating is associated with a skin depth where most of the power absorbed by conductor [1,6]. The skin depth is defined by equation 2.4.

$$\delta = \sqrt{\frac{1}{\pi \mu f \sigma_e}} \tag{2.4}$$

When the radius of the particle is equal to or smaller than the skin depth, power is dissipated in the whole region of the particle. Critical frequency is calculated simply by replacing δ in equation 2.4 with the particle radius R.

$$f_{crit} = \frac{1}{\pi R^2 \mu \sigma_e} \tag{2.5}$$

f_{crit} of 10nm diameter Au particle is about 2×10^5 GHz with the bulk electrical conductivity and the fact $\mu \approx \mu_0$. Generally "low frequency" denotes the frequency much smaller than f_{crit}[6,9]. In the frequency regime, the particle is uniformly heated. One thing to note is that the wavelength of incident magnetic field should be much longer than the particle size to simplify the analysis. This assures that the whole particle is in the uniform magnetic field at each moment[9] (figure 2.1). In addition, the validity of equation 2.2 is not guaranteed if the wavelength becomes comparable with the atomic length scale[10]. The wavelength of ~GHz magnetic wave (in the low frequency range) is order of sub-meter, much larger than our particle's size. Thus using low frequency such as GHz or MHz range of magnetic field is acceptable for the nanocluster antenna experiment.

(a) $R > \lambda$ (b) $R < \lambda$
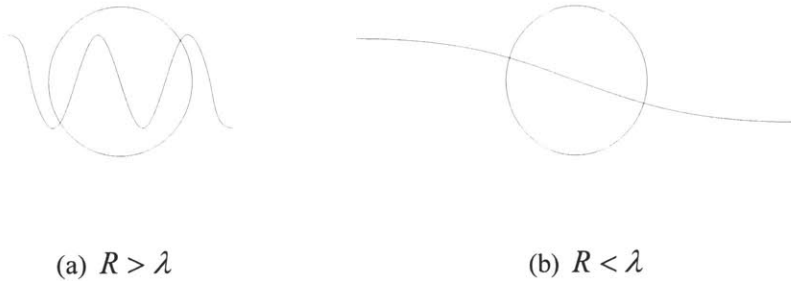
Figure 2.1 Phase of magnetic wave inside particle.

The results of applying equation 2.3 to cylindrical and spherical particle are listed in table 2.1 with their limit forms for low frequency and high frequency[6,9]. An analytical kinetics solution is also available for the case that the particle size is much smaller than mean free path(MFP) of electron ranging 10~100nm[9,11] in metal. It is assumed that there are no scatterings between electrons, and the electrons are diffusively reflected at the wall(i.e., equal probability for all directions of reflection, regardless of the incident angle). Low frequency is still assumed, too. The result is given in table 2.1.

	Cylindrical particle [W/particle]	Spherical particle [W/particle]
classical solution	$\dfrac{\pi H_0^2 R l_{sample}}{\sigma_e \delta \left| J_0\left[(1-j)\dfrac{R}{\delta}\right]\right|^2} Re\left\{(j-1)\cdot J_1\left[(1-j)\dfrac{R}{\delta}\right]\cdot J_0\left[(1+j)\dfrac{R}{\delta}\right]\right\}$	$\dfrac{3\pi R^5 \omega^2 \mu^2 (\mu_0 H_0)^2 \sigma_e \left\{\dfrac{1}{2}u(S+s)-C+c\right\}}{(\mu-\mu_0)^2\left\{\left(\dfrac{u^2}{2}+1\right)C+\left(\dfrac{u^2}{2}-1\right)c-u(S+s)\right\}+(\mu-\mu_0)\mu_0\dfrac{u^3}{2}(S-s)+\mu_0^2\dfrac{u^4}{4}(C-c)}$
$f \ll f_c$	$\dfrac{1}{16}\sigma_e\omega^2\mu^2 H_0^2 \pi R^4 l_{sample}$	$\dfrac{1}{15}\sigma_e\omega^2\mu^2 H_0^2 \pi R^5$
$f \gg f_c$	$\dfrac{H_0^2}{\sigma_e\delta}\pi R l_{sample}$	N/A
MFP>R $f \ll f_c$	$\dfrac{\omega^2\mu^2 H_0^2 e^2 n\pi R^5 l_{sample}}{20 m_e v_f}$	N/A

Table 2.1 Analytical solutions on induction heating per each cylindrical and spherical particle[6,9].
Note) n ; electron concentration ε_f : Fermi level m : mass of electron

We may compare two formulas of cylindrical particle at low frequency condition. The ratio of kinetics' solution to classical solution is $\dfrac{4ne^2 R}{5m_e\sigma_e v_f}$. From the bulk properties of gold, the ratio is about $(2\times10^7)\cdot R$ without dimension. For example, kinetics solution of 10nm gold may gives only about 1/10 of volumetric energy dissipation compared to classical solution. But we should remember that this comparison is only valid for the particle size less or similar with MFP of electron due to the assumption made on the particle dynamics solution. In addition, electrical properties of nanoparticle may be different from those of macroparticle, so the ratio changes. However, we can accept that classical solution may be considered as an upper limit of the amount of possible heat generation.

2.1.3 Hysterisis loss and relaxation loss

We assumed linear relationship between B and H in the previous chapter (equation 2.2). However, magnetic material actually shows hysterisis behavior. It is well

known that the enclosed area of the hysterisis curve gives the energy loss during a one cycle of H change. Paramagnetic materials like gold have a linear response, and thus do not yield hysterisis loss. In addition, nanosize magnetic particles sometimes result in single magnetic domains that are superparamagnetic. Since the volume of a nanoparticle is very small, its magnetization can be easily perturbed by thermal fluctuation. But transition to superparamagnetism depends on not only the size, but also frequency and magnetic field strength[5].

Figure 2.2 shows how hysterisis curve changes with particle dimension and the amplitude of magnetic field. Data are given for unit weight of the particles[5]. Relatively bigger particles having multi-magnetization domains are used. Figure 2.2(a) explains the size dependence of hysterisis. We can also infer from figure 2.2(b) that if the magnetic field intensity is not strong enough to change the magnetization direction of each single domain, hysterisis behavior will not be observed. Once the hysterisis is saturated at certain field strength, higher H doesn't give bigger hysterisis area, too.

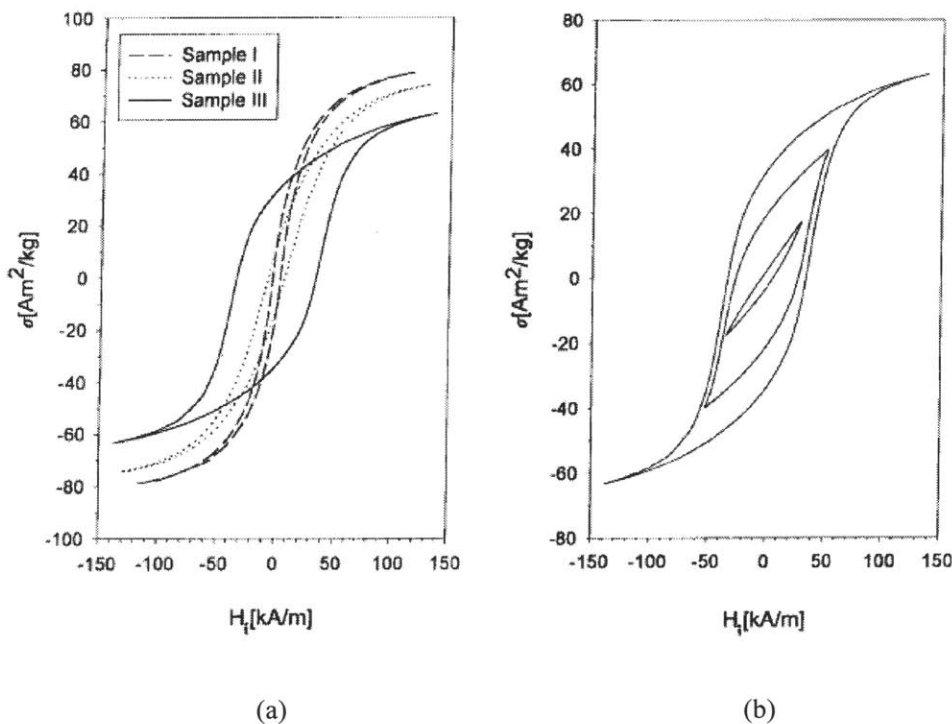(a)   (b)

Figure 2.2 (a) Saturated hysterisis loops of sample1: ~350nm, sample2: ~250nm, sample3: ~50nm x 1500nm, rod shape (b) Hysterisis of sample 3 for three different loop amplitudes measured at 50Hz. Copied image[5]

Generally very small magnetic particle gives superparamagnetism as described earlier. From the measurement, Fe_3O_4 particles below 10nm in diameter don't have any hysterisis loop. But still there is loss of power comparable with anisotropic particles according to some experiment[5,12,13]. Neel relaxation and Brownian relaxation can explain these heating phenomena for non-hysterisis particle.

An external alternating magnetic field supplies energy and assists magnetic moments in overcoming the energy barriers between magnetization states. This energy is dissipated when the particle moment relaxes to its equilibrium orientation. The loss caused by this mechanism is called Neel relaxation[5,14]. Relaxation time for this system is determined by the ratio of anisotropy energy KV to thermal energy k_BT, if only two anti-parallel orientations of the magnetic moment m are assumed for simplicity.

$$\tau = \tau_0 \exp\left(\frac{KV}{k_BT}\right) \tag{2.6}$$

τ_0 is on the order of nanosecond and V is the particle volume. For the oscillating external magnetic field, the analytical solution for the resultant power is given below[5].

$$P = \frac{(mH_0\omega T)^2}{2\tau kTV(1+\omega^2\tau^2)} \quad \left[W/m^3\right] \tag{2.7}$$

At the low extreme of ω, P is proportional to ω^2, thus P decreases as ω becomes smaller. For very high ω, it becomes constant(equation 2.8). It is interesting that induction heating of pure paramagnetic particle gives the same frequency dependence(see Table 2.1).

$$P = \frac{(mH_0)^2}{2\tau kTV} \quad \left[W/m^3\right] \tag{2.8}$$

For nanofluid, another type of relaxation occur due to rotational Brownian motion of the magnetic particles[5,6]. Particles are rotating under alternating magnetic field because of their magnetization. This results in viscous drag between particle surface and fluid. Equation 2.9 shows Brownian relaxation power loss of each particle[6]. To reach the result, classical equations of fluid mechanics are used, though their validity at nanoscale is

14

somewhat questionable. In addition, low frequency(ω <10^5rad/s) is assumed to make sure smooth and full rotation of particles.

$$P = \frac{3}{4}\omega\mu_0 H_0^2 \qquad \left[W/m^3\right] \tag{2.9}$$

To combine Neel relaxation and Brownian relaxation, Brownian relaxation time constant τ_B[5,15] may come from the order of magnitude relation between thermal fluctuation and rotational energy dissipation $k_B T \sim 8\pi\eta R^3 \cdot \omega \sim \dfrac{8\pi\eta R^3}{\tau_B}$.

$$\tau_B = \frac{8\pi\eta R^3}{k_B T} \tag{2.10}$$

The effective relaxation time constant τ_{eff} can be approximated as equation 2.11[5].

$$\tau_{eff} = \frac{\tau \cdot \tau_B}{(\tau + \tau_B)} \tag{2.11}$$

From equation 2.6, we expect larger Neel relaxation time constant compared to Brownian relaxation time for bigger particle due to its exponential term. τ_{eff} converges to τ_B in the case. On the contrary, τ is dominant for very small particles(~nm).

In summary, Neel relaxation is a major concern at high frequency(~MHz or higher) and for the particles with small size, whereas Brownian relaxation is important for low frequency and big particles. Hysterisis loss rapidly disappears as the particle size decreases due to superparamagnetism. Thus the induction heating mechanism of magnetic particle with the size in the order of some nanometer is mainly governed by Neel relaxation. (Note: the term "low frequency" mentioned here is only in mathematical sense. It differs from the frequency that is smaller than critical frequency of induction heating(equation 2.5) which is described in chapter 2.1.2)

2.2 Nanoscale heat transfer mechanism

2.2.1 Introduction

We have seen some theories for heat generation in the previous chapter. Now we need to figure out how the generated heat propagates to the surrounding medium. Two major variables characterizing heat transfer are temperature and heat flux. Most questions evolving from heat transfer basically request to show those two values by use of the given parameters such as thermal conductivity, specific heat, density, and so on. It is very well known that there are three modes of heat transfer; heat conduction, convection, and radiation. Heat conduction is governed by Fourier's law(equation 2.12), and can be formulated further to the diffusion equation(equation 2.13) by use of energy conservation law[16,17]. Convection phenomena can be described as a simple form(equation. 2.14), but convection heat transfer fundamentally comes with fluid motion, which requires solving Navier-Stokes equation(equation 2.15) at the same time[17,18]. So heat transfer coefficient h cannot be achieved easily. Radiation equation is also described in a short form(equation. 2.16), but the energy conservation equation for radiation is an integral equation rather than differential equation, which is a main cause to make hard to solve coupled heat transfer modes' problem.

$$q'' = -k\nabla T \quad (W/m^2)$$ \hfill (2.12)

$$\nabla(k\nabla T) + q''' = \rho C_p \frac{\partial T}{\partial t}$$ \hfill (2.13)

$$q'' = h(T - T_\infty)$$ \hfill (2.14)

$$\rho \frac{D\overline{u}}{Dt} = \mu\nabla^2\overline{u} - \nabla p + \rho(\overline{g} + \overline{f})$$ \hfill (2.15)

$$q'' = \varepsilon\sigma(T^4 - T_\infty^4)$$ \hfill (2.16)

One thing to note is that conduction and convection equation are based on continuum medium assumption. For example, a bulk of water is a group of a huge number of water molecules. Though the governing equations are expressed in differential forms, we

cannot take too small control volume for the analysis. If we do, we probably see the molecular properties of water rather than those of bulk. We need to set lower limit that allows differential analysis without loss of bulk properties. Generally the limit for fluid motion is believed to be order of micron or less. Similar explanation can be made for heat conduction, too. Thus if the length scale of the system is at or below this value, we may not be able to use classical equations. There is also a limit for time scale. Classical equation cannot be used for very short time scale such as femtosecond laser case because there is not enough time for heat carriers' relaxation[10]. Since there has been recently much concern about nanoscale devices and structures, necessity of more precise prediction of thermal behavior has grown up. The theories in classical regime failed to describe nanoscale heat transfer phenomena as explained above, thus new concept emerged and is now widely accepted. This will be reviewed below.

2.2.2 Nanoscale heat transfer between parallel plates

Semiconductor industries are confronting the challenge of putting more and more circuits per unit area and reducing the thickness of device layers. Highly integrated circuits generate a considerable heat, motivates nanoscale heat transfer study. Not surprisingly, studies first came with the analysis of heat transfer between two parallel plates, essential for the design of semiconductor layers[19-22]. Heat conduction phenomena between parallel plates can be explained by particle transport concept. Major heat carriers of metal are electrons and phonons, while those of dielectric materials are phonons[10]. At sufficiently large length and time scales that avoid violating continuum and relaxation limits, there are enough scattering between heat carriers in the medium. Energy can propagate by collisions between carriers. So we can use equation 2.12 and equation 2.13, and this type of transport is diffusive. On the other hand, if there is no scattering between heat carriers, the carriers emitted from one side do not lose their energy until they reach the other side. This mechanism is very similar with the radiation phenomena between two parallel plates filled with transparent media. Photons travel from one plate to the other without any obstacles. There are no scatterings or no absorptions of photons. This gives the idea that we can use radiation formula for the no scattering limit, called Casimir limit or ballistic limit[21]. Since

the existence and frequency of scattering between heat carriers is very important, we need to consider mean free path(MFP) of the heat carriers an indicator to show whether the system is in ballistic regime or diffusive regime. MFP in solid medium can be roughly calculated by equation 2.17 [11].

$$k = \frac{1}{3}Cv\Lambda \qquad (2.17)$$

The phonon MFP is 1~100nm in general, but electron MFP depends on free electron density. Therefore electron MFPs are much longer in dielectric materials than in metals[10]. In other words, heat conduction in a dielectric material is dominated by phonon transport, but both phonons and electrons affect the conduction mechanism in metal. For the case that the length scale of object is comparable with MFP, both diffusive and ballistic behavior should be considered. Boltzmann transport equation (BTE) is used to derive an equation of phonon radiative transfer (EPRT)[20] and a hyperbolic equation called the Cattaneo equation[23] is also suggested. The BTE (equation 2.18) and EPRT mainly describes scattering and absorption in media, and both BTE and Cattaneo equation(equation 2.19) have effective relaxation time scale τ_R to explain short time scale phenomena. τ_R is defined by Λ / v, usually the order of picoseconds to nanoseconds based on a typical phonon of 1000m/s[10]. Since τ_R changes with the mean free path Λ, MFP affects the solutions of the two equations. If we get rid of scattering terms from equation 2.18 and 2.19, the remaining is simply continuity equation or Fourier law. Researchers simply add one more term representing scattering and to get more realistic solutions.

$$\frac{\partial f}{\partial t} + v \cdot \nabla f = \left(\frac{\partial f}{\partial t}\right)_{scat} \simeq -\frac{f - f_0}{\tau_R} \qquad : BTE \qquad (2.18)$$

$$\tau_R \frac{\partial q''}{\partial t} + q'' = -k\nabla T \qquad : Cattaneo \qquad (2.19)$$

The steady state solution of EPRT for two parallel plates filled with dielectric media is given in equation 2.20[20].

$$q'' = \frac{\sigma_p\left(T_1^4 - T_2^4\right)}{\left(\dfrac{3}{4}\dfrac{L}{\Lambda} + 1\right)} \qquad (2.20)$$

The steady state temperature distributions from three different regimes are also shown in Fig 2.3.

Diffusive Transport
$$q'' = -k\nabla T$$

Diffusive-Ballistic Transport
$$q'' = \frac{\sigma_p\left(T_1^4 - T_2^4\right)}{\left(\dfrac{3}{4}\dfrac{L}{\Lambda} + 1\right)}$$

Ballistic Transport
$$q'' = \sigma_p\left(T_1^4 - T_2^4\right)$$

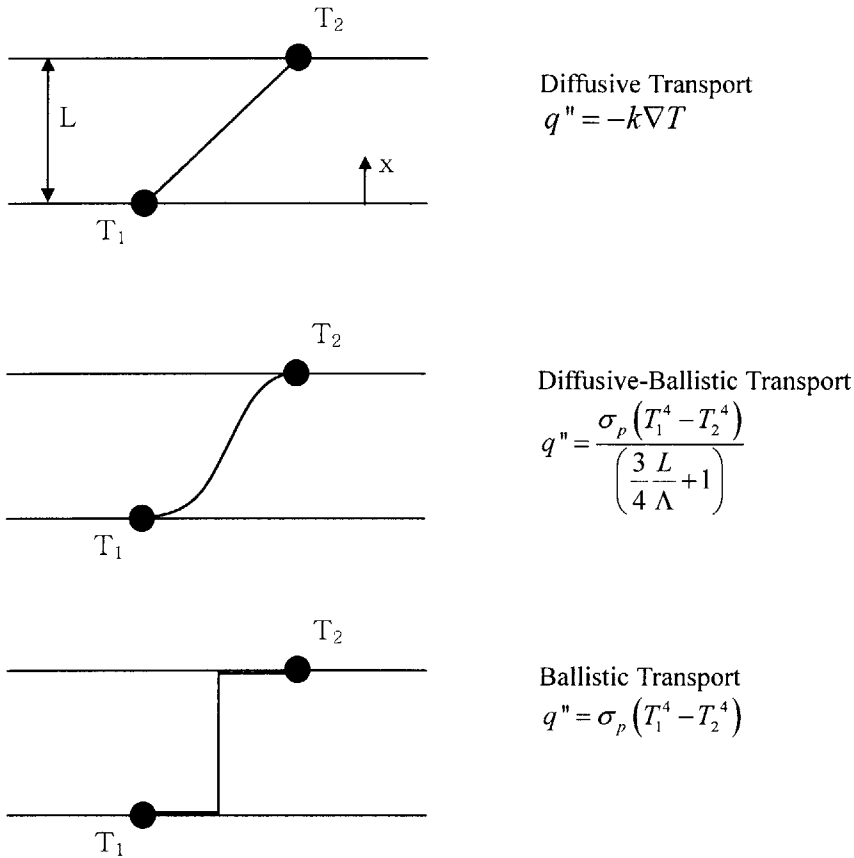Figure 2.3 Schematic diagrams quantitatively show the steady-state temperature profiles. In the regime of diffusive or ballistic phonon transport[21].

In ballistic transport regime, there is no energy exchange between hot and cold phonons, thus local equilibrium does not exitst. At every position, the number density of hot and cold phonons is uniform and the conceptual temperature can be defined by averaging the phonon

energies of both kinds. This temperature is different from the classical temperature, which is based on local equilibrium.

Figure 2.4 shows numerical solution of transient temperature distribution in diamond slab with 0.1μm thickness initially at T=T_2[21]. EPRT, Fourier law with energy conservation, and hyperbolic heat equation are used. MFP can be calculated by equation 2.17 from material properties.
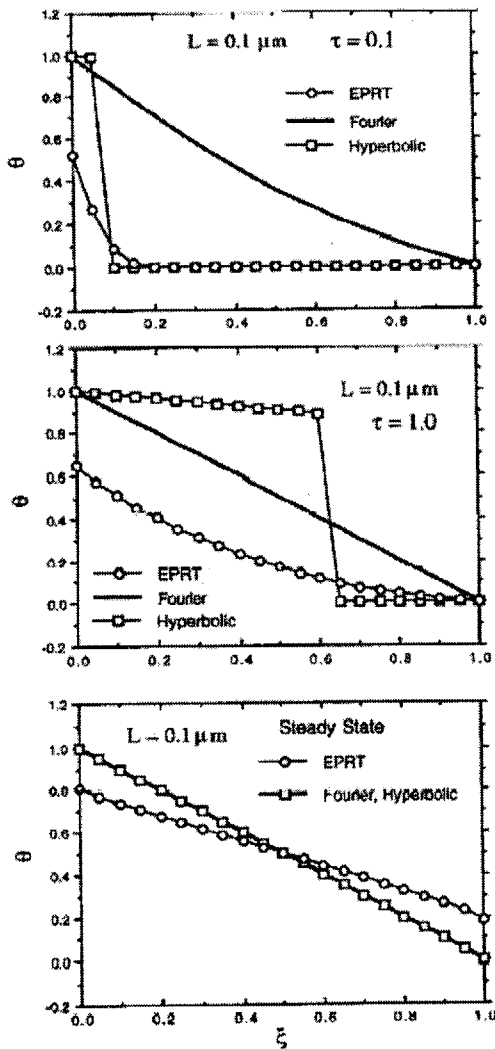
Figure 2.4 Variation of dimensionless temperature profiles predicted by the EPRT, Fourier law, and hyperbolic heat equation as functions of dimensionless time. Thickness of the diamond film is 0.1μm. The film was initially at T=T_2. Copied image[21]

$$\theta = \frac{T - T_2}{T_1 - T_2}$$

$$\tau = \frac{t}{\tau_R}$$

$$\xi = \frac{x}{L}$$

Geometry of the parallel plates is given in Figure 2.3

The result shows that Fourier law(equation 2.12 and 2.13) cannot give a temperature profile

20

varying with time. The classical time constant to reach steady state can be expressed as

L^2 / α and is much smaller than τ_R in this problem mainly due to a very small L. This is

not a realistic description. If we look at the other two solutions, after very short time such

as $\tau = 0.1$(or t=0.1 τ_R), the diamond thin film is still at initial temperature T_2 except near

x=0. For $\tau = 1$, or t= τ_R, hyperbolic equation shows an unrealistic temperature profile. There

is a temperature jump in the middle of the medium. On the contrary EPRT shows the most

acceptable result. Temperature profile rises as time progresses. One thing to note is that

there are always temperature jumps at both walls according to the EPRT solution. The

discontinuities do not disappear even at steady state. This is from the fact that EPRT is

based on the radiation equation, where there is a thermal resistance right next to the wall,

depicting the medium gas's ability to absorb emitted energy from the wall.

2.2.3 Nanoscale heat transfer from particle to medium

Heat transfer from uniform sphere to medium was studied with BTE and EPRT[24].
The author discovered the fact that the solution is identical with that of parallel plates

analysis if the gap size L is replaced with the particle radius R. This analysis assumes that

phonons are the only heat carriers in the medium, similar to the two parallel plates problem.

Particle size parameter

$$\tau_1 = \frac{r_1}{\Lambda}$$
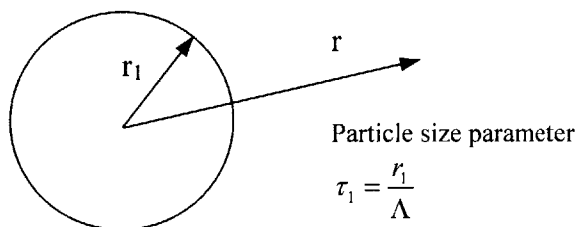
Figure 2.5 Schematic diagram of the heat transfer from sphere to host medium

The particle size parameter τ_1 (figure 2.5) plays an important role. Large τ_1 means

that the size of the particle is much bigger than MFP, and this allowing enough phonon

scattering around the surface of sphere within the length scale of the particle size. On the

contrary, there are only a few scattering events if τ_1 is small. Figure 2.6 illustrates two

extreme cases of τ_1.

(a) $r_1 < \Lambda$ (b) $r_1 > \Lambda$
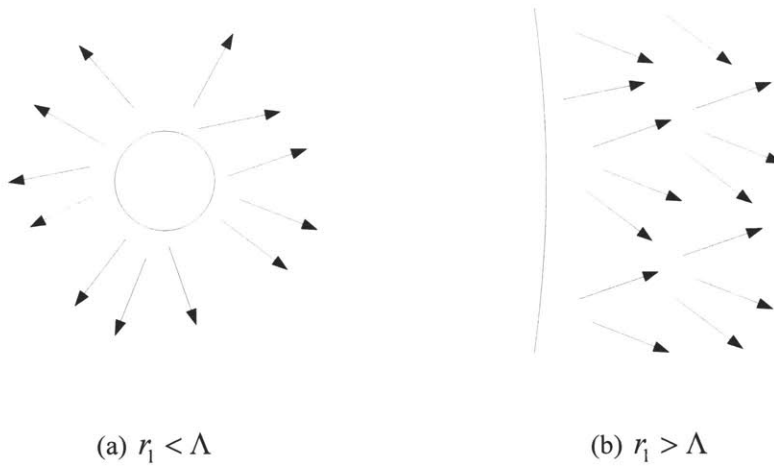
Figure 2.6 Schematic diagrams of phonon scattering for two different τ_1's.
The length of an arrow is proportional to the phonon MFP in host medium

The steady state solution is given in Figure 2.7[24]. The host medium is initially at T_2, and the particle surface is at T_1. Like the parallel plates problem, there is a temperature discrepancy at the interface(r/r_1=1). The nondimensional temperature rise φ is 0.5 at the interface for the low extreme of τ_1, which means that the temperature was calculated by the average of two kinds of phonons coming from the surface of the sphere and infinite medium without any scattering. For high τ_1, the result is almost identical with the solution from Fourier's law.
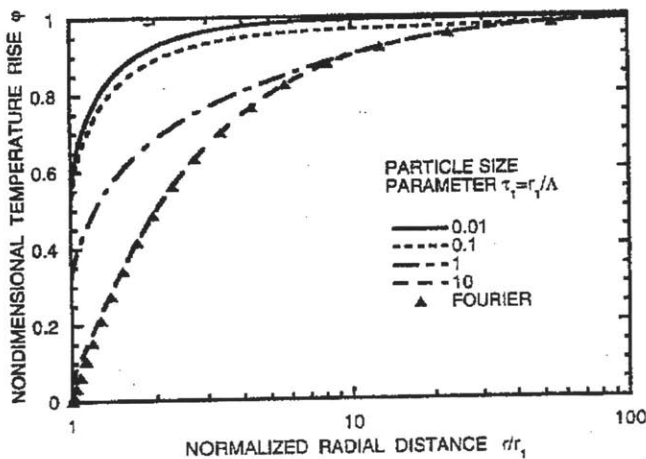
Figure 2.7 Distribution of nondimensional equivalent temperature φ.
Copied image[24]

$$\varphi = \frac{T - T_1}{T_2 - T_1}$$

22

Through further analysis, effective thermal conductivity k_{eff} was approximated as equation 2. 21[24],

$$\frac{k_{eff}}{k} = \frac{\left(3\tau_1/4\right)}{\left(3\tau_1/4\right)+1}$$ (2.21)

where k is the bulk thermal conductivity. Figure 2.8 describes how the effective thermal conductivity changes with different length scales[24]. It can be induced that if τ_1 is larger than about 10, we can use the thermal conductivity of bulk states, but still not for very near field (within a few MFP) to the particle. For smaller τ_1, effective thermal conductivity decrease rapidly, due to reduced scattering of phonons. Equation 2.21 is shown in fig. 2.8 (circles) and matches very well with exact numerical solution. Generally speaking, nanostructures have a smaller thermal conductivity[25] compared to macrostructures, thus cooling problem of nano-devices becomes more difficult. This creates a challenge for the device industry.

Figure 2.8 Normalized effective thermal conductivity as a function of particle size parameter. Copied image[24]

The mean free path of water is ~0.3nm (also based on equation 2.17). If we deal with 5nm or 10nm diameter particles in water, we may use the classical heat conduction equation for the particle to medium transport. But for much smaller particles (<1~2nm), we need to get th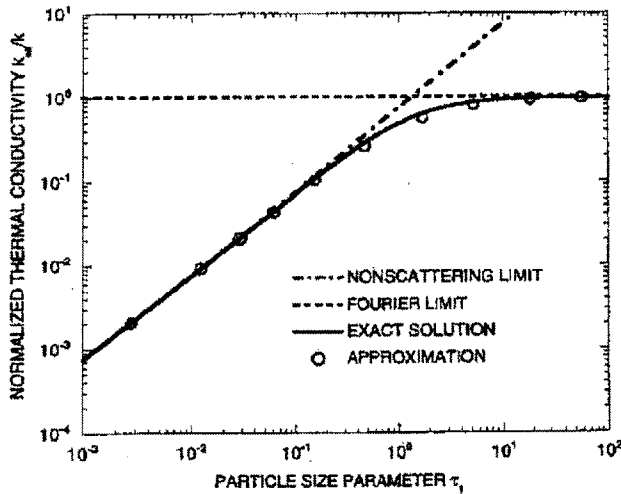e answer directly from EPRT. Another thing to note is that we need to check whether there is possibility for the initiation of convection heat transfer. But for our concerns, which are about 5nm or 10nm particles, we do not need to take into account convection phenomena according to some research on nanofluid[26-33]. The research has shown that fluid with well-dispersed nanosize particles has higher thermal conductivity compared to pure fluid. The authors mainly use a hot-wire technique, and the diameter of the wire is typically microns. From these measurements, non-existence of convection within a certain time scale was evidenced around the wire. So we may ignore convection around particles in much smaller size scale.

2.2.4 Interface thermal resistance and other material properties

The methods used in ch.2.2.2 and 2.2.3 do not consider the interface thermal resistance. It is natural that there is a certain amount of contact resistance at a discontinuity of a material structure. If we deal with large system, the interface resistance is usually ignored because the resistance of the media is dominant. Problems occur in nanoscale structures, where the ratio of the interface area to the volume of material becomes substantially large. The diffuse mismatch model(DMM)[34] and lattice dynamical model(LD)[35] have been developed to explain irregular phonon movement at the interface. The main concept of DMM is that phonons are randomly and elastically scattered at the interfaces with a transmission coefficient given by the relative density of vibrational states on the two sides of the interface[25]. On the contrary, LD assumes that there is no scattering at the interface and directly deals with the lattice structure of the media. Figure 2.9 shows some interface thermal conductance data of microfabricated structure from experiment and the theories[25]. The right hand side vertical axis shows equivalent material thickness that gives the same amount of thermal resistance. It is simply the thermal conductivity divided by interface conductance. DMM and LD were used to model the Al/Al_2O_3 interfaces. The graph shows that both theories overestimate the conductance (i.e., by underestimating the

24

resistance). One remarkable thing is that for most combinations of two solid materials making an interface, the interface conductances fall into a very narrow range. At room temperature, the high extreme thermal conductance is only ~5 times larger than the lowest conductance[25]. They are generally on the order of 100MW/m²K.
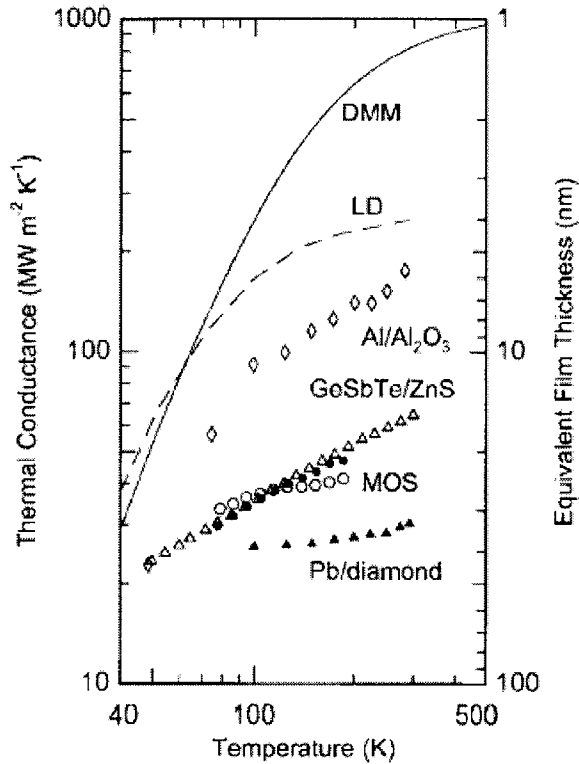
Figure 2.9
Thermal conductance vs.
temperature. Copied image[25].

Thermal conductance
$h_s (MW / m^2 K)$

Equivalent thickness
$$l_{eq} = \frac{k}{h_s}$$

Our concern is much more about solid to liquid interfaces, and the above data are from solid-solid interfaces. If we recall that DMM considers phonon transmission coefficients for both sides of the interface, we can infer that the thermal resistance between the solid and liquid is very high because phonons in liquid are rarely initiated by the interfacial collision of phonons in the solid[10]. However, the other extreme on thermal conductance can be explained by liquid layering. In liquid-particle mixtures, the liquid molecules close to a particle surface are known to form layered structures, and behave much like a solid[36,37], which gives a smooth change of properties at the interface and less thermal resistance. The size of layering is known to be order of some nanometers[36]. The validity of the theory for liquid layering is still under study.

25

2.3 Application to Au particle and water system

In chapter 2.2.3, we concluded that if we use 5nm or 10nm Au particles dispersed in water, we can use bulk thermal conductivity and classical diffusion equation for water region. Temperature discontinuities originating from nanosize effect also can be neglected. But importantly we still have to take into account the interface thermal resistance, which also causes an abrupt temperature change at the interface.

For heat transfer analysis of particle to water system, we need some more physical properties. The density of gold particles of diameter ~10nm is almost the same as that of bulk gold, because the atomic structure of Au particles is similar with that of bulk[38,39]. For the specific heat, we need to separate phonon specific heat and electron specific heat in the case of metals. The specific heat of phonon is proportional to T^3 when T is low, but it is nearly constant when T is much larger than Debye temperature (170K for gold). Whereas electron specific heat is proportional to T for the whole temperature range, but also is a function of the particle size. The change of the electron specific heat is due to the difference in energy levels and the density of states[11]. Figure 2.10 shows the temperature dependence of the specific heat of bulk gold[10]. We can infer that phonon specific heat is dominant for overall range of temperature, thus specific heat of gold at room temperature is nearly constant regardless of size change. The conclusion throughout the above is that we can use density and specific heat of bulk water and gold, whereas bulk thermal conductivity is only for water until now. Classical Fourier law and diffusion equation is still valid in water if we use some nanometer sized gold. In addition, interface resistance may be considered.
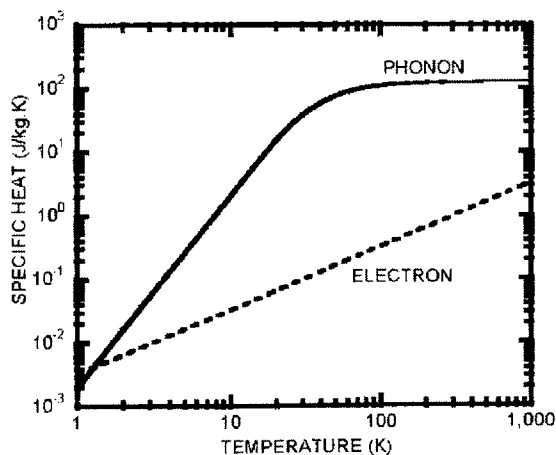

Figure 2.10 Specific heat of gold calculated for phonon and electron. Copied image[10]

A classical solution for heat conduction from heated sphere to ambient material is well developed in literature [7,40,41]. All the materials are initially at T=0 and the sphere starts to generate uniform q''' $[W/m^3]$ after t=0. Governing equations are spherical forms of equation 2.13 and boundary conditions are very common in heat transfer textbook [17]. They are listed in equation 2.21-27, and the geometry is given in figure 2.11. But some complicated algebra rises from Laplace's transform and its inverse transform. In addition, no interfacial resistance is assumed during the analysis, which gives continuous temperature profile at the interface. The interface resistance will be discussed later. Here the particle is considered bulk, which is not quite true for the thermal conductivity of nanoparticle.

$$\frac{1}{\alpha_1}\frac{\partial T_1}{\partial t} = \frac{1}{r^2}\frac{\partial}{\partial r}(r^2\frac{\partial T_1}{\partial r}) + \frac{q'''}{k_1}, \quad 0 \le r < R \tag{2.21}$$

$$\frac{1}{\alpha_2}\frac{\partial T_2}{\partial t} = \frac{1}{r^2}\frac{\partial}{\partial r}(r^2\frac{\partial T_2}{\partial r}), \quad r > R \tag{2.22}$$

$$T_1 = T_2 = 0 \ at \ t = 0 \qquad \text{: initial condition} \tag{2.23}$$

$$T_1 = T_2 \ at \ r = R \qquad \text{: temperature continuity} \tag{2.24}$$

$$k_1\frac{\partial T_1}{\partial r} = k_2\frac{\partial T_2}{\partial r} \ at \ r = R \qquad \text{: heat flux matching at interface} \tag{2.25}$$

$$T_1 : finite \ as \ r \to 0 \tag{2.26}$$

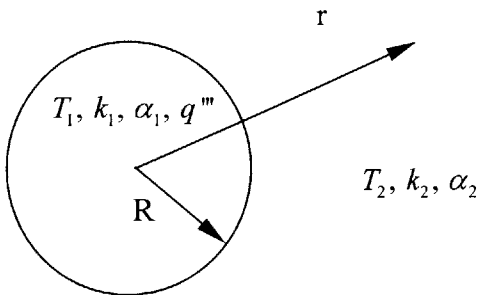$$T_2 : finite \ as \ r \to \infty \tag{2.27}$$

Figure 2.11 Geometry of heat transfer problem. Initially the sphere is at T_1 and the medium is at T_2

27

The transient solutions are given in equation 2.28 and 2.29,

$$T_1 = \frac{q'''R^2}{k_1}\left\{\frac{1}{3}\frac{k_1}{k_2} + \frac{1}{6}\left(1 - \frac{r^2}{R^2}\right) - \frac{2bR}{r\pi}\int_0^\infty \frac{\exp(-y^2 t/\gamma_1)}{y^2}\right.$$

$$\left. \cdot \frac{(\sin y - y\cos y)\sin(ry/R)}{[(c\sin y - y\cos y)^2 + b^2 y^2 \sin^2 y]}dy\right\} \quad (0 \le r < R) \tag{2.28}$$

$$T_2 = \frac{q'''R^3}{rk_1}\left\{\frac{1}{3}\frac{k_1}{k_2} - \frac{2}{\pi}\int_0^\infty \frac{\exp(-y^2 t/\gamma_1)}{y^3}\right.$$

$$\left. \cdot \frac{(\sin y - y\cos y)[by\sin y \cdot \cos \sigma y - (c\sin y - y\cos y)\sin \sigma y]}{[(c\sin y - y\cos y)^2 + b^2 y^2 \sin^2 y]}dy\right\} \quad (r > R) \tag{2.29}$$

where $b = \frac{k_2}{k_1}\sqrt{\frac{\alpha_1}{\alpha_2}}$, $c = 1 - \frac{k_2}{k_1}$, $\gamma_1 = \frac{R^2}{\alpha_1}$ and $\sigma = \left(\frac{r}{R} - 1\right)\sqrt{\frac{\alpha_1}{\alpha_2}}$. An Interesting thing to note is

that the time scale γ_1, for the overall system to reach steady state, depends on α_1 only. Considering the thermal diffusivity of bulk gold(table 2.2), it is about 0.2 picosecond for 10nm gold. But this time scale is not accurate. The phonon relaxation time constant τ_R was already discussed in chapter 2.2.2, and the time scale for classical heat transfer equation should be much larger than τ_R. Due to insufficient phonon scattering, the real time scale to steady state is expected to be much larger than γ_1.

The steady state solution can be achieved by taking $t \to \infty$ from equation 2.28 and 2.29.

$$T_1 = \frac{q'''R^2}{k_1}\left\{\frac{1}{3}\frac{k_1}{k_2} + \frac{1}{6}\left(1 - \frac{r^2}{R^2}\right)\right\} = \frac{q'''R^2}{3k_2} + \frac{q'''R^2}{6k_1}\left(1 - \frac{r^2}{R^2}\right) \quad (0 \le r < R) \tag{2.30}$$

$$T_2 = \frac{q'''R^2}{3k_2}\frac{R}{r} \quad (r > R) \tag{2.31}$$

Volumetric power generation q''' can be from Table 2.1 by being divided by particle

volume, or equation 2.7~9 can be considered if we use magnetic particles. An illustration of equation 2.30 and 2.31 is given in figure 2.12. One assumption is that particle solution is dilute enough to neglect the interactions between the particles. The maximum temperature is $\frac{q'''R^2}{3k_2}\left(1+\frac{k_2}{2k_1}\right)$ at the center of the sphere, and the interface temperature is $\frac{q'''R^2}{3k_2}$. At $r = 2R$, temperature decreases to a half of the interface temperature. If k_1 is substantially larger than k_2, particle's center temperature converges to the interface temperature, thus we can consider that the whole particle is nearly isothermal in that case. We can also see that temperature change linearly depends on q'''. Generally experimental or theoretical data of power generation are accurate only to an order of magnitude, resulting in a considerable difference in the temperature profile. For example, even if the real temperature increase is a few degrees, estimates for the resulting temperature could range from $<1^{\circ}C$ to $100\,^{\circ}C$. This give rises to the necessity of direct measurement of temperature. These ideas will be discussed in chapter 3.
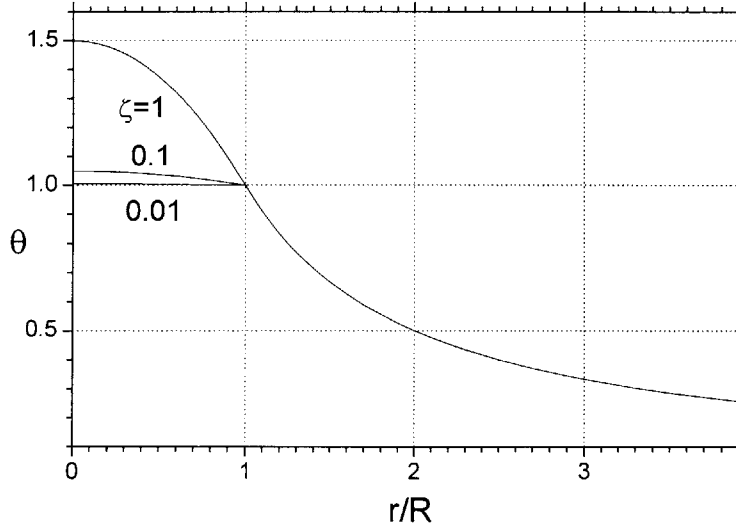
Figure 2.12 Temperature distribution of particle and medium, where

$$\theta = \frac{\Delta T}{\left(\frac{q'''R^2}{3k_2}\right)} \quad,\quad \zeta = \frac{k_2}{k_1}$$

Now an Au particle - water system is taken into account. Physical properties[11,16] are from bulk properties of gold and water at room temperature(table 2.2).

	Gold (material 1)	Water (material 2)
$k\ [W/m \cdot K]$	317	0.61
$\alpha\ [m^2/s]$	1.27×10^{-4}	1.47×10^{-7}
$\rho\ [kg/m^3]$	19280	996
$\zeta = k_2/k_1$	1.92×10^{-4}	-
$\sigma_e\ [\Omega^{-1}m^{-1}]$	4.55×10^7	-
$\mu\ [H/m]$	$\sim 4\pi \times 10^{-7}$	-

Table 2.2 Physical properties of bulk Au and water at 300K[11,16]

Due to its very small ζ, gold particle is expected to be nearly isothermal. Actually we have not discussed if we can use the classical equation and bulk thermal conductivity to describe the particle. But even if we consider the size effect, particles are still isothermal due to no phonon scattering inside the particles(figure2.3). So the ideas from both regimes give the same pictures for the particle's temperature profile. Another important question is that which power dissipation formula should be used. We may use the classical one for the spherical particle in table 2.1. We should divide it by the particle volume to get q''' (equation 2.32). Though no kinetics formula for sphere is available in table 2.1, we may guess that the classical one has higher value by considering the cylindrical particle's solution.

$$q''' = \frac{P}{(volume)} = \frac{\frac{1}{15}\sigma_e \omega^2 \mu^2 H_0^2 \pi R^5}{\frac{4}{3}\pi R^3} = \frac{\sigma_e \omega^2 \mu^2 H_0^2 R^2}{20} \qquad (2.32)$$

30

We may take into account hysterisis, Neel relaxation, and Brownian relaxation loss for magnetic particles, but not for Au particles. The interface temperature now becomes equation 2.33.

$$\Delta T_{int} = \frac{q''' R^2}{3k_2} = \frac{\sigma_e \pi^2 \mu^2 f^2 H_0^2 R^4}{15k_2} \tag{2.33}$$

Unfortunately, ΔT_{int} of 10nm gold under 1GHz, 20kA/m magnetic field is just 2×10^{-11} °C according to equation 2.33. To get 20 °C as temperature increase, we need 10μm Au particles under the same magnetic field condition. But it was reported that even 1.4nm gold can heat up oligos attached on its surface[1]. It is hypothesized that other unknown heating mechanisms may be present, or the given formula cannot describe the actual temperature. Instead of gold particle we may use magnetic particles. Due to high magnetic permeability, ΔT_{int} of magnetic particle is an order of larger than that of Au particle. Also we can expect hysterisis loss and relaxation loss. Though low frequency gives less power, we probably cut down magnetic field frequency for magnetic particles because other parameters will compensate. In addition, high frequency magnetic waves may do harm on biological systems.

Finally, we need to check the effect of interface thermal conductance h_s given in chapter 2.2.4. If there is considerable thermal resistance, there will be a temperature discontinuity between the interfaces. The energy balance equation at the interface is given in equation 2.34.

$$q = h_s (T_{R-0} - T_{R+0}) \cdot (4\pi R^2) = q''' \cdot (\frac{4}{3}\pi R^3) \tag{2.34}$$

Combined with $\Delta T_{int} = \frac{q''' R^2}{3k_2}$, the sudden temperature drop at the interface is as below.

$$T_{R-0} - T_{R+0} = \Delta T_{int} \frac{k_2}{Rh_s} \tag{2.35}$$

From chapter 2.2.4, it was discussed that thermal conductance for solid-solid interface is usually about order of 100MW/m²K. If we treat the Au-water interface the same as solid-solid contact, $T_{R-0} - T_{R+0}$ becomes order of the same as ΔT_{int} from equation 2.35. Interface conductance between Solid-liquid may be even less than that of solid-solid interface, because there are much less phonon initiations in water right next to the interface which are resulted from inner particle's phonon collisions(i.e., phonon transmission coefficient from solid to liquid is very small). Thus there can be very big temperature difference at the interface for Au-water system. Figure 2.13 shows this schematically. If the resistance is extremely high, generated energy will be trapped in the particle. The particle temperature will rise significantly and may affect the bond between the particle and oligo. However, liquid layering theory [36,37] gives an opposite explanation. Nanofluid gives enhanced mixture thermal conductivity even bigger than prediction from theories, and some researchers suggest that it is due to the increase of effective size of the particle resulted from liquid layering [28-30]. However, this still needs more investigation. In addition, some other mechanisms for thermal conductivity enhancement are being suggested. To get a more precise answer, we may try diffuse mismatch analysis with the transmission coefficient from solid to water, while it has not been revealed clearly.
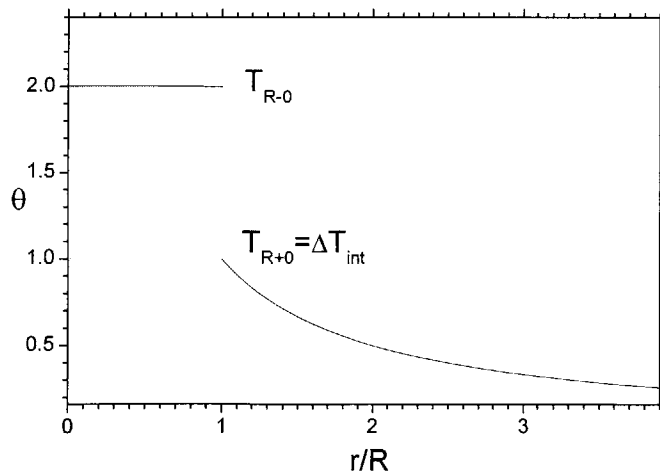
Figure 2.13 Temperature distribution of particle and medium with interface resistance

$$\theta = \frac{\Delta T}{\left(\dfrac{q'''R^2}{3k_2} \right)} \; , \; \zeta = \frac{k_2}{k_1} = 1 \; , \; \frac{k_2}{Rh_s} = 1$$

2.4 Nomenclatures for chapter 2

B	Magnetic flux density
C_v	Vloumetric specific heat
f	Frequency
H	Magnetic field strength $[A/m]$
h_s	Interface thermal conductance $[MW/m^2K]$
J	Currenty density
k_B	Boltzmann constant
k	Thermal conductance $[W/mK]$
l	Length
m_e	Effective mass of electron
n	Free electron concentration
q	Heat generation $[W]$
q''	Heat flux $[W/m^2]$
q'''	Volumetric heat generation $[W/m^3]$
R, r_1	Particle radius
t	Time
v	Velocity of phonon
v_f	Fermi velocity
α	Thermal diffusivity $[m^2/s]$
δ	Skin depth of induction heating
ε_f	Fermi energy $(= m_e v_f^{\,2}/2)$
η	Fluid viscosity $[kg/ms]$
Λ	Mean free path
λ	Wavelength
μ	Magnetic permeability $(= \mu_r\mu_0)$ $[H/m]$
μ_0	Vacuum permeability $(= 4\pi \times 10^{-7} H/m)$
σ_e	Electrical conductivity $[\Omega^{-1}m^{-1}]$
μ	Magnetic permeability $(= \mu_r\mu_0)$ $[H/m]$
τ	Neel relaxation time scale

τ_B	Brownian relaxation time scale
τ_{eff}	Effective relaxation time scale
τ_R	Effective phonon relaxation time scale $(= \Lambda / v)$
τ_1	Particle size parameter $(= r_1 / \Lambda)$
ω	Angular velocity $(= 2\pi f)$ $[rad / s]$
θ, φ	Non-dimensional temperature

Chapter 3: Direct measurement of temperature profile in nanoscale

Through chapter 2, some possible explanation was given for the temperature profile around gold particles in water under alternating magnetic field. But there is a limitation due to an inexact estimation on the amount of power. Biological activity is very sensitive to temperature, thus a wrong estimation of power will result in undesired effects. This motivates a direct measurement of the actual temperature profile. We already know that classical methods for temperature probing such as thermocouples and IR cameras are not applicable to nanometer-size systems. We need data points at every ~nanometer intervals, but that level of resolution has not yet been achieved. In addition, particles in liquid experience Brownian motion. Since the particle is the reference point of the coordinate as well as the heating source, we have to trace the position of the freely moving particle and gather some temperatures within the reference frame relative to the center of the particle. Due to the reasons DNA temperature probing is a possible solution. Oligos are directly attached to particles, and the oligos have special temperature indicators. The information from the indicators will be translated into the temperature profile. In this chapter, brief description on the project is given, though it should be addressed to be the future work. In addition, some literature about DNA's persistence length will be reviewed. To use a DNA strand as a ruler between metal particles and indicators, rigidity of the DNA should be considered.

3.1 Fluorescence measurement toward temperature probing
3.1.1 Introduction

Fluorescence is one of the most common methods in modern biological science. Fluorescence is the phenomenon in which absorption of light of a given wavelength by a fluorescent molecule is followed by the emission of light at longer wavelengths. There are many kinds of fluorophores having their own excitation and emission spectrum. Figure 3.1 shows excitation spectrum and emission spectrum of fluorescein [42].

35
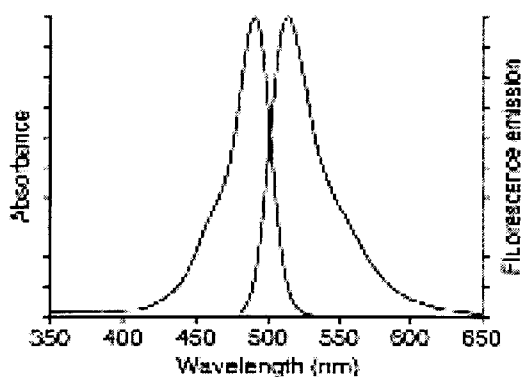
Figure 3.1 Excitation and emission spectrum of Fluorescein.
Copied image [42]

The most remarkable advantage of fluorescence over other optical techniques is its sensitivity. Absorbance measurements are generally done with micromolar oligo concentration, whereas fluorescence reliably works with nanomolar or even picomolar concentration. Another good point is the availability of fluorescence quenching. A quencher is a molecule that has strong absorption at similar wavelength of a certain fluorophore's emission peak. If both molecules are close enough to each other then fluorescence cannot be seen. Table 3.1 shows some common fluorophores and quenchers [43]. It is also known that metal particles are very strong quenchers[44,45]. For example, a 10nm gold particle has an absorbance peak at 520nm. Thus fluorescein, with an emission peak at 520nm, is mostly quenched by nearby gold particles.

Fluorophore	Max. Abs.	Max. Emi.
6-FAM	495nm	517nm
CY3	550	570
CY5	650	667
CY5.5	675	694
Fluorescein	495	520
HEX	537	553
JOE	520	548
LightCycler Red 640	625	640
LightCycler Red 705	680	705
Oregon Green 488	495	521
Oregon Green 500	499	519
Oregon Green 514	506	526
Rhodamine	564	603
Rhodamine6G	524	557
Rhodamine Green	504	532
Rhodamine Red	570	590
ROX	581	607
TAMRA	550	576
TET	521	538
Texas Red	589	610

Quencher	Max. Abs.	Max. Emi.
BHQ-1 Dark	535nm	None
BHQ-2 Dark	579	None
BHQ-3 Dark	672	None
DABCYL Dark	453	None
DABCYL-dT Dark	453	None
QSY-7	560	None
TAMRA	550	576nm

Table 3.1 Maximum absorbance and emission wave length of fluorophores and quenchers in common use[43]

3.1.2 Description for the experiment

Figure 3.2 depicts the temperature probing experiment. One DNA strand has thiol group at 5' end, and a quencher at 3' end. This is hybridized with shorter complementary strand that has fluorophore at 5' end. Two different kinds of double-stranded DNA(dsDNA) are given in figure 3.2. The hybridized part of each DNA is identical, but single-stranded part (offset strand) has a different length. After conjugated with gold particle through thiol group, it is placed under magnetic field with known strength and frequency. Since the probability of dehybridization is higher for the DNA with shorter offset strand, we can get higher fluorescence intensity from it due to reduction of fluorescence quenching. Note that if we attach quenchers and fluorophores in the other way(i.e., fluorophore on the strand conjugated to Au and quencher on the complementary strand), the particle may quench the fluorophore regardless of the temperature.

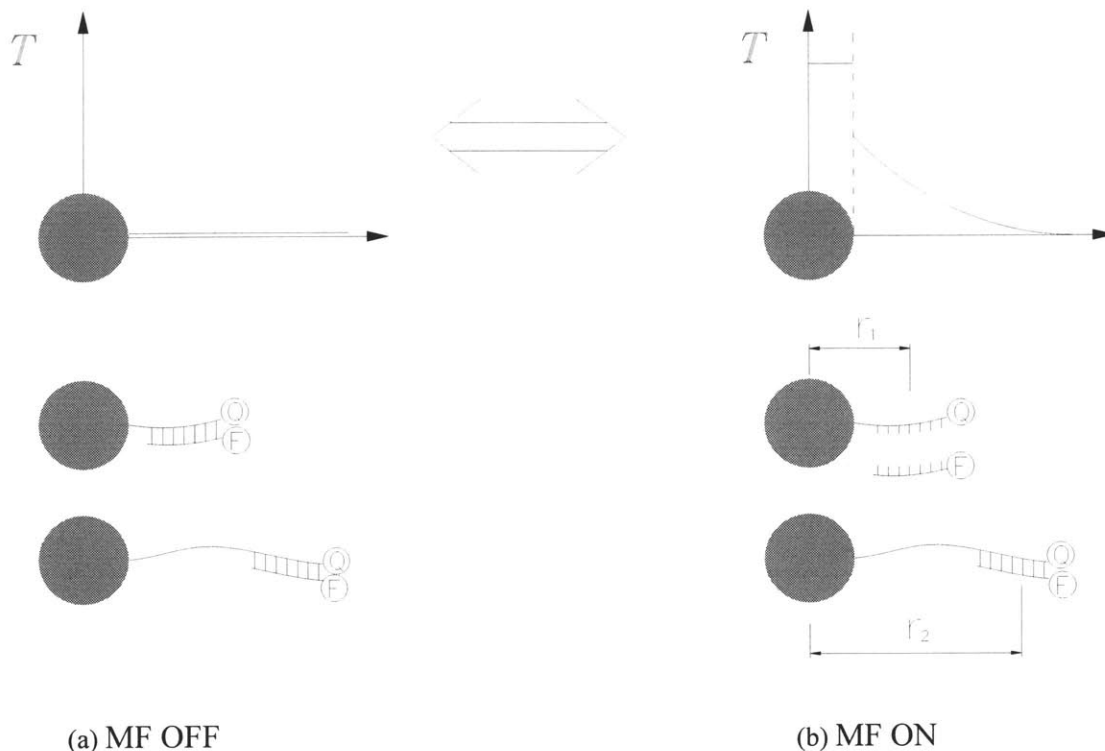<div style="text-align:center">(a) MF OFF   (b) MF ON</div>

Figure 3.2 Description of the temperature probing experiment for the case
(a) when the alternating magnetic field is turned off and (b) turned on.

As a reference experiment we need to measure the fluorescence of the solution at different bulk temperature. By comparing the intensities we are able to infer the temperature around the double-stranded part of the DNA.

But there exist some actual problems for using the above method. One is DNA adsorption to the gold surface[46,47]. The phosphate groups as well as the functional groups such as amines and carbonyls in DNA bases (see figure 3.3) can donate electron pairs to the particle surface, thus DNA strands wrap up the gold particle. Since the length of DNA strand determines the distance from the heat source to a double stranded part, it is essential to keep the strand detached from the particle. We may use a homogeneous thymine series as an offset strand because they have the smallest affinity to gold surface compared with other bases[46]. But we need to develop a more general method to treat unspecific sequence for future application such as antisense. Some researchers reported that 6-mercapto-1-hexanol

(MCH) effectively replace the DNA adsorption site on flat gold surface[48]. It motivates the same treatment on gold particle but requires much more precise reaction control, because gold particles are easily aggregated due to charge loss upon MCH reaction. Chapter 4 will deal with the MCH treatment on Au particle-DNA conjugates, and their conformation change by MCH reaction is confirmed by Ferguson plot analysis.
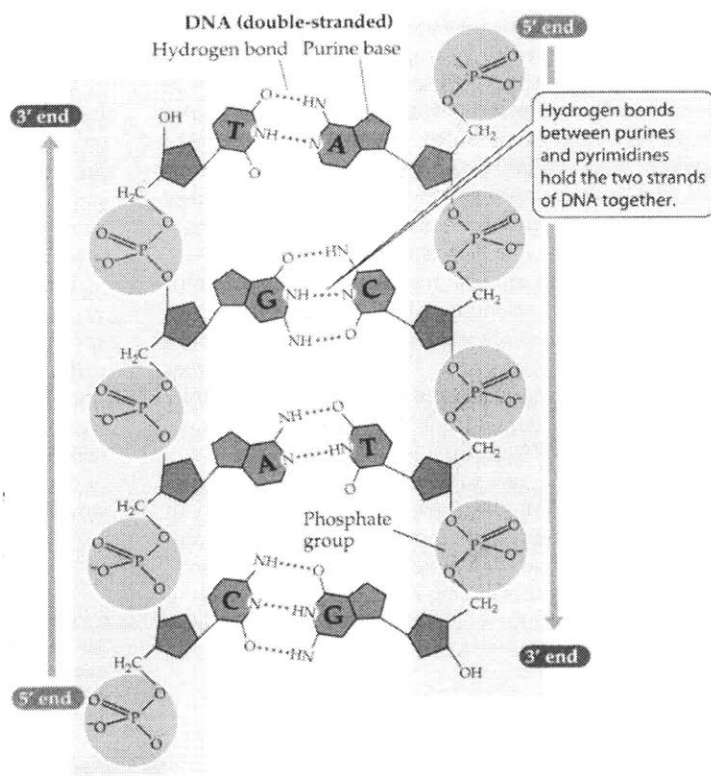

Figure 3.3 Chemical structure of double-stranded DNA[49]

Once the DNA is in a radial conformation, we have to measure the actual distance from the particle center to the dsDNA, the actual temperature probe. Average end-to-end length of polymers can be achieved by persistence length analysis. It is reviewed in chapter 3.2.

3.2 DNA persistence length

3.2.1 Introduction

To measure or to calculate the persistence length of polymer has been an extensive topic for the last a few decades because the rigidity of polymer is a main parameter for its conformation. Persistence length is conceptually defined as the length over which the average deflection of the polymer axis caused by thermal agitation is one radian[50]. More rigorously, it is the sum of the average projections of all chain segments on the direction of a given segment or simply the first segment[51,52]. Due to recent emphasis on biology and biotechnology, the persistence length of biomolecules including DNA has become an important issue. Conformational changes of biomolecules are directly related with their activity, and inversely we can influence them by changing external force and stress, etc[53]. For example, a single-stranded DNA(ssDNA) has different ability to hybridize with its complementary strand according to their conformation. Also when transcriptions occur, double stranded DNA(dsDNA) partially open their double helix structures. We may be able to control these phenomena with the exact picture of the behavior.

3.2.2 Basic theories on persistence length

Generally two kinds of persistence length are mentioned in DNA related research. One is from enthalpic contribution and the other is entropic contribution[54,55]. The latter is due to the statistical distribution of DNA conformation, while the former is mainly because of the rigidity of DNA itself. In general, short DNA strands have fewer number of possible conformations, thus the enthalpic persistence length dominates. Some other researchers using DNA electrophoresis employ different classifications such as intrinsic and electrostatic contributions[56-59]. Since DNA strands have charges on their backbones, ionic strength of the medium becomes very important to describe charge-screening behavior, which induces reduction of charge repulsion between DNA bases. In any case, the overall persistence length p is considered as the sum of the two persistence lengths, because the entropic or electrostatic term gives additional stiffness.

40

$$p = p_0 + p_e \qquad (3.1)$$

p_0 denotes the enthalpic (or intrinsic) persistence length, and p_e means the entropic (or electrostatic) persistence length for different situation. When electrostatic contribution to the persistence length is considered, Debye layer κ^{-1} becomes important parameter. It is associated with Bjerrum length[59,60],

$$l_B = \frac{e^2}{\varepsilon k_B T} \qquad (3.2)$$

the distance where the electrostatic energy between two counter ions with unit charge e is the same as thermal fluctuation $k_B T$. Then κ^{-1} can be expressed as

$$\kappa^{-1} = \frac{1}{\sqrt{4\pi z(z+1)l_B c}} \qquad (3.3)$$

For intrinsically stiff polymer such as short DNA strand, p_e is approximated as [59,60]

$$p_e = \frac{l_B \lambda^2}{4z^2} \left(\kappa^{-1} \right)^2 \qquad (3.4)$$

where z is the valency of the ions, λ is line charge density, and c is the concentration of ions[59,61]. Though the equation is not applicable to all cases, it shows that smaller Debye length, which can be caused by high salt concentration or high valency, induces less electrostatic stiffness.

One more description on the classification is found in other literature[50,62], where static(p_s) and dynamic(p_d) contribution of persistence length are mentioned. Dynamic contribution is the persistence based on thermal fluctuation. Hence the static persistence length may contain all the other effect such as intrinsic and electrostatic contributions. The authors defined the overall persistence length in a different way[50,62].

41

$$\frac{1}{p} = \frac{1}{p_s} + \frac{1}{p_d}$$ (3.5)

It is understood from the formula that both contributions making the DNA "pliable" give rise to the decrease of the overall persistence length.

From the understanding of persistence length, some theories for the conformation of polymer chains were suggested. Among them, Freely Jointed Chain (FJC) model and Worm Like Chain (WLC) model are most commonly used. FJC model assumes that polymer is a serious of orientationally independent statistical segments(Kuhn segments)[63]. On the contrary, WLC model consider polymers continuous, thin and flexible chains, which give[50,63]

$$\langle \vec{t}(s) \cdot \vec{t}(s + \Delta s) \rangle = \exp\left(-\frac{\Delta s}{p}\right)$$ (3.6)

where $\vec{t}(s)$ is the unit tangential vector of the contour. Persistence length p is involved in WLC model. From well established theories, the root-mean-square end-to-end length under the absence of force is given as

$$R = \left\langle \left|\vec{R}\right|^2 \right\rangle^{1/2} = \sqrt{Nb^2} = \sqrt{Lb} \qquad : \text{FJC}$$ (3.7)

$$R = \sqrt{2}p\left[\frac{L}{p} + \exp\left(-\frac{L}{p}\right) - 1\right]^{1/2} \qquad : \text{WLC}$$ (3.8)

For FJC, the chain length L can be expressed as the product of the Kuhn length b and the number of Kuhn segments N. It also can be written as simply monomer length times the number of monomers, but practically not for FJC. Sometimes b of FJC is treated as $2p$ due to the fact that R of WLC becomes close to $\sqrt{2Lp}$ as L becomes much larger than p. More specifically, the probability distribution of R for WLC model is known by[64]

$$P(r,t) = \frac{4\pi A r^2}{(1-r^2)^{9/2}} \exp\left(\frac{-3t}{4(1-r^2)}\right)$$ (3.9)

42

Where

$$A = \frac{4(3t/4)^{3/2}\exp(3t/4)}{\pi^{3/2}\left(4+\dfrac{12}{(3t/4)}+\dfrac{15}{(3t/4)^2}\right)} \qquad (3.10)$$

with $t = L/p$ and $r = R/L$.

All these equations can be argued by excluded-volume interaction, which means that a position in space cannot be occupied by two monomers simultaneously[58,65]. When the volume scale of polymer Ld^2 (d: polymer diameter) is much larger than the cube of Kuhn length, the excluded-volume may affect the end-to-end size of the polymer.

$$R = N^{\nu}b = L^{\nu}b^{1-\nu} \qquad (3.11)$$

ν is known as Flory exponent, approximately equal to $0.6^{58,65,66}$. Also if κ^{-1} is comparable to or bigger than the polymer diameter, the excluded volume becomes the order of $(\kappa^{-1})^3$, and the end-to-end length may follow a different rule[58].

We can also find some useful approximations for force-extension relation[55,60,67].

$$R = L\left[\coth\left(\frac{2Fp}{k_bT}\right)-\frac{k_bT}{2Fp}\right]\left(1+\frac{F}{K}\right) \qquad : \text{FJC} \qquad (3.12)$$

$$F = \left(\frac{k_BT}{p}\right)\left[\frac{1}{4(1-R/L+F/K)}-\frac{1}{4}+\frac{R}{L}-\frac{F}{K}\right] \qquad : \text{WLC} \qquad (3.13)$$

Above equations contain enthalpic contribution term F/K that is due to elastic stretching of polymer structure itself. But practically this term is negligible in case of random coil[67]. An approach for more exact solution is given in literature[60,67]. Based on WLC model, energy stored in chain can be expressed as

$$E_{WLC} = \int_0^L \left(\frac{K_B}{2}\left|\frac{\overline{dt(s)}}{ds}\right|^2 - F\cos\theta(s)\right)\cdot ds \qquad (3.14)$$

where K_B is bending stiffness of polymer. The first term of the integrand is the stored

energy due to bending, and the relation $p = K_B / k_B T$ holds. The Boltzman factor $e^{-E_{WLC}/k_B T}$ is used to get partition function Z, and finally the relation

$$\frac{R}{L} = \frac{k_B T}{L} \frac{\partial \ln Z}{\partial F} \tag{3.15}$$

is used for numerical calculation of force-extension relation. By comparing with equation 3.13, the author [67] simply added correction terms up to 7th order,

$$F = \left(\frac{k_B T}{p} \right) \left[\frac{1}{4(1-l)} - \frac{1}{4} + l + \sum_{i=2}^{7} a_i \cdot l^i \right] \tag{3.16}$$

where $l = R / L - F / K$.

Important thing to note is the fact that force-free end-to-end length or force-extension relation contain persistence length term, though its definition in the formula changes somewhat(e.g., a half of Kuhn length or bending stiffness over thermal fluctuation). Thus we can get persistence length of DNA by comparing the theoretical models with some experimental result showing the above relations. Also it can be more exactly compared with direct simulation of FJC or WLC model.

3.2.3 Double-stranded DNA's persistence length

There have been numerous researches on dsDNA's persistence length, and it has been a typical way of the research to figure out the relationships between force and DNA's configuration. One way of DNA stretching is to use electrophoresis. External electric field gives rise to motion of DNA, and the force is balanced by drag force from relative fluid motion[56]. Thus DNA moves with constant velocity during electrophoresis(or at rest). DNA is stained by fluorescence materials, which gives the information about its conformations. From FJC model, a relationship is given as[56]

$$R = \frac{1}{\alpha} \ln \left[\frac{\sinh \alpha L}{\alpha L} \right] \tag{3.17}$$

44

where $\alpha = E_0 \lambda b / k_B T$, E_0 is electric field strength and λ is line charge density. Thus $E_0 \lambda b$ is a local force acting on one Kuhn segment. The author compared experimental data of λ-phage DNA with equation 3.17 with varying λ, finally got $\lambda = 15e^-$ per $p(= b/2)$. To get the persistence length through FJC simulation, electric field was removed to compose a random coil. By measuring the average end-to-end length, $p \sim 80$nm was achieved. The approaches in the article may be claimed because excluded volume effect was not considered. Since κ^{-1} is of order 1~3nm for highly charged polymer such as DNA in general salt condition[58,59], effective diameter of DNA is similar to $d + 2\kappa^{-1}$ rather than just d. Electro-osmotic flow may affect the force balance in the case [68].

Actually there have been some arguments[58,60,68,69] on the situation involving both hydrodynamic force and electrostatic force, because the electro-osmosis flow is sometimes underestimated. In addition, fluid motion induced by one monomer (or a part equivalent to Kuhn length) also may affect other monomers. We cannot say that the local force balanced by fluid drag is simply $E_0 \lambda b$ [58,68]. At the same time, the total force is not $E_0 \lambda L$. A more realistic overall force balance is given below[58,68].

$$F - \xi(v_{fluid} - \mu_0 E_0) = 0 \tag{3.18}$$

μ_0 is the mobility under the absence of external fluid flow. When external fluid velocity is zero(i.e., most gel electrophoresis cases),

$$F = \xi \mu_0 E_0 = 6\pi \eta R_h \mu_0 E_0 \sim \eta R_g \mu_0 E_0 \tag{3.19}$$

where R_h is hydrodynamic radius and R_g is the radius of gyration originated from intrinsic viscosity of polymers[70]. Considering equation 3.7 or 3.11, and 3.19, we can reach the below relation.

45

$$F \sim R_g \sim R \sim L^{0.5} \ (\text{or } L^{0.6}) \tag{3.20}$$

Note that the mobility μ_0 is almost constant when reptation occurs regardless of its length[71]. This force-chain length behavior was confirmed experimentally by use of fluid flow[72], by fixing one end of DNA with optical trapping. The experiment shows that the free end of DNA is not very stable [60,72]. The fluctuation is caused by a variation in the hydrodynamic drag force as the DNA conformation changes [72].

Since there is uncertainty for the conformation when we let one or both ends of the DNA free, direct stretching of both ends may be preferred to get clearer picture. Due to recent technology such as optical trap, it is possible to control both force(~pN) and position in very precise manner. Very popular experiment was done on B-form λ-Phage DNA to get enthalpic contribution to the persistence length[66]. As described earlier, stretching random coiled DNA mainly depends on entropic feature, whereas nearly linear polymer is subjected to enthalpic behavior. Equation 3.12 or 3.13 can be recalled. The author reported that force-extension experiment gives linear relationship up to F ~60pN. Around 65pN, the DNA suddenly stretched to ~1.7 times its B-form contour length, which means the rupture of one of its strands. Twisted coil becomes straight at this stage. But it recovers its shape when released, though there is a certain time scale for the recovery. It is stated that the required force for the sudden behavior becomes small when ionic strength becomes low. Low degree of charge screening causes electrostatic repulsion between DNA backbones. Another experiment with optical tweezer[55] shows that multi-valent ions in solution gives low persistence length compared to mono-valent ions. It is in agreement with the explanation given on equation 3.3 and 3.4. In 10mM Na^+ salt condition, the persistence length achieved is 47nm, but reduces to 39nm in 100μM Mg^{2+} solution, even lower concentration compared to Na^+. But no further drop of the persistence length is observed for higher salt condition, thus we can infer that the intrinsic persistence length is about 39nm.

Regarding with equation 3.5, cryo-electron microscopy can be used to instantaneously immobilize and image the DNA[50]. dsDNA trapped between 40~50nm slabs

46

is rapidly cooled with the rate of 10^6K/s. It is fast enough to capture a single state out of many different dynamic fluctuations. By comparing the actual DNA conformation with numerical simulation of equation 3.6, dynamic persistence p_d is given as 80nm. If we assume the overall persistence length is 50nm (or 45nm from this article), then the static persistence length is about 130nm from equation 3.5. This static persistence length is much longer than the values called "intrinsic" from the above. The author explains that the overall persistence length is basically containing the pliability originated from thermal fluctuation, thus if we get rid of the effect, DNA becomes stiffer.

Besides the methods mentioned above, some other imaging and stretching methods such as scanning force microscopy[63,73], moving meniscus[74], etc. Through numerous researches, the persistence length of dsDNA is believed to be of order 50nm with some variation.

3.2.4 Persistence length of single-stranded DNA

In general, single-stranded DNA(ssDNA)'s have much smaller persistence length compared to dsDNA which compose sturdy double helix structure. From the force-extension relation given in equation 3.12 and 3.13, we can see that a small persistence length requires higher force to stretch, but results in small end-to-end length according to equation 3.7 and 3.8.
Stretching experiment with optical tweezers was done on single-stranded DNA(ssDNA)[66]. The procedure is identical with that of dsDNA experiment given above. In the early stage of stretching, ssDNA is much more contractile than dsDNA, but overstretch behavior is similar with dsDNA because only one of the two strands is dominant during the dsDNA overstretching. From the experiment and FJC model, calculated p ($= b$ /2) was only 0.75nm which is comparable to the length of two bases only.

The ssDNA's persistence lengths are calculated for different salt conditions and chain length[57]. It was done thourgh measuring the diffusivity of each random coil ssDNA, by use of fluorescence recovery after photobleaching(FRAP). Stokes-Einstein relation is given in equation 3.21.

$$D_s = \frac{k_B T}{6\pi\eta R_h} = \frac{k_B T}{6\pi\eta(\xi R_g)} \qquad (3.21)$$

Radius of gyration R_g is given as[70]

$$R_g = \frac{R}{\sqrt{6}} = \frac{\sqrt{2Lp}}{\sqrt{6}} = \sqrt{\frac{Lp}{3}} \qquad (3.22)$$

for long WLC. Intrinsic viscosity is considered in equation 3.22, and excluded volume effect comes in ξ, rather than in the end-to-end length. The author[57] took $0.5<\xi<0.664$ from various sources. In addition, L is the product of the number of bases N_0 and monomer length b_0 (~0.43nm for ssDNA in this article, but may be argued). From equation 3.21 and 3.22, we can see $D_s \sim N_0^{-0.5}$ for fixed p. If excluded volume effect is considered in end-to-end length, $D_s \sim N_0^{-v}$ should hold. Since the diffusivity data exactly fit in these relation [57,66], ssDNA length dependent behavior of p was not observed. It is understood from the fact that the smallest ssDNA used for the experiment is $N_0=280$, long enough to be WLC.

An important point made by the experiment is that the persistence length of ssDNA highly depends on ionic strength(figure 3.4) [57]. Data from another article[66] agree with the graph in the high salt condition, which gives intrinsic persistence length.
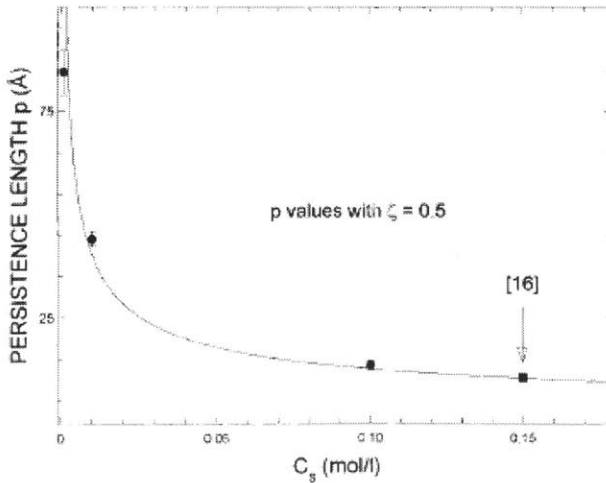

Figure 3.4 Persistence length change with the ion concentration C_s(mol/L) with ξ =0.5. The arrow denotes the data from [66]. Copied image[57].

48

Rather than using randomly sequenced long chain, we may be interested in short ssDNA. However, it is difficult to image the actual contour because of its very small size. Recently fluorescence resonance energy transfer (FRET) experiment was carried out with short ssDNA (N_0 =10~70) wholly composed of thymines. Figure 3.5 shows a schematic of the DNA used for the experiment. One advantage of the experiment is that we do not concern about each strand, but measure the overall intensity from the bulk solution.
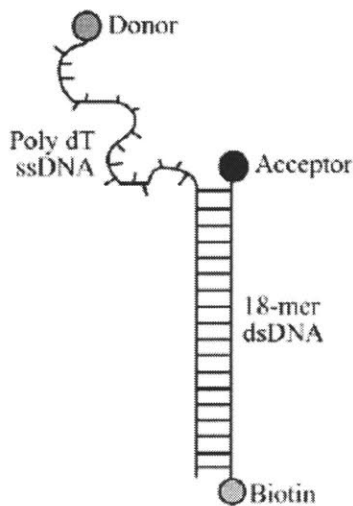

Figure 3.5 A Schematic of dT_{N_0} tailed, fluorescence labeled DNA. N_0 varies from 10 to 70. Copied image[64].

The energy transfer efficiency E is defined below[64,75].

$$E = \frac{1}{\left[1+\left(\dfrac{R}{R_0}\right)^6\right]}$$

(3.23)

R is donor-acceptor distance which is equal to the average end-to-end length of dT_{N_0} from the figure 3.5, and E is the fraction of the donor's excitation resulting in the excitation of the acceptor. Characteristic distance R_0 can be defined as a theoretical formula depending on salt condition and the characteristics of donor and acceptor[75], but it is about 6nm for various NaCl concentrations (25mM~2M) and Cy3-Cy5 pair used in this experiment. If we consider the probability distribution of the end-to-end length given in equation 3.9, we can

modify the transfer efficiency as

$$E = \int_0^1 P(r) \frac{1}{\left[1+\left(rL/R_0\right)^6\right]} dr \qquad (3.24)$$

where $r = R/L$. To get chain length L, the monomer length is assumed to be 0.63nm, calculated from computerized molecular construction software. This value is a little different from that of [57], but sequence dependent persistence behavior will be explained later.

Figure 3.6 shows the change of E with the number of bases and salt concentration. Each line for different salt concentration comes from the numerical simulation with the optimal persistence length that gives the best fit with the experiment data of E. This also shows that high salt concentration induces intrinsic persistence length due to charge screening of DNA backbones. The range of the persistence length is 1.5nm~3nm, similar with the diffusivity experiment on long chain[57].
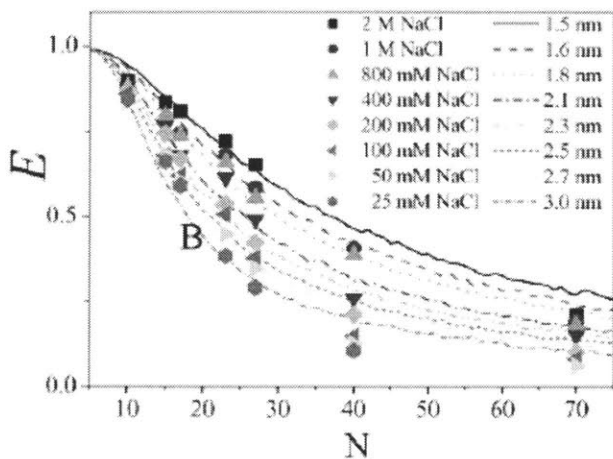

Figure 3.6 FRET efficiencies for different sizes of DNA and salt concentration. Image from [64].

Short and homogeneous serious of thymines were also used in other experiments[63,76].

To get detectable conformation change, dT_{N_0} is introduced only in the middle of dsDNA(figure 3.7). Double stranded parts are nearly straight since their lengths are within the range of the persistence length of dsDNA.
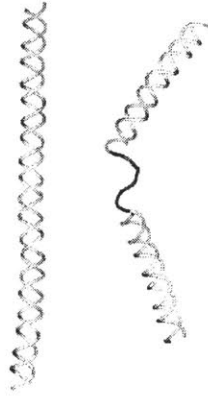

Figure 3.7 A schematic of ssDNA having dsDNA wings. Image from [76].

The DNA chain given in figure 3.7 is comprised with sections of different persistence length. The overall end-to-end length is related with all the p's, section lengths, and angles of each joint. The formula is given in the literature[63].

$$R_{(\beta_1,...,\beta_N:p_1,...,p_N)} = \sqrt{2}\left\{\sum_{n=1}^{N+1} p_n^2\left[\frac{L_n}{p_n}-\left(1-e^{-L_n/p_n}\right)\right]\right.$$
$$+\sum_{n=1}^{N} p_n \cdot p_{n+1}\cos\beta_n\left(1-e^{-L_n/p_n}\right)\left(1-e^{-L_{n+1}/p_{n+1}}\right) \tag{3.25}$$
$$\left.+\sum_{n=1}^{N-1}\sum_{m=n+2}^{N+1} p_n \cdot p_m\cos\left(\sum_{i=n}^{m-1}\beta_i\right)\left(\prod_{j=n+1}^{m-1}e^{-L_j/p_j}\right)\left(1-e^{-L_n/p_n}\right)\left(1-e^{-L_m/p_m}\right)\right\}^{\frac{1}{2}}$$

N+1 is the total number of sections and N is the number of joints. p_n and L_n are the persistence length and section length of nth segment. β_n is the angle between the tangent vectors of nth and (n+1)th segment at the joint. Smooth chain gives β_n=0. The only

unknown is ssDNA's persistence length, and all other parameters are supposed to be known including end-to-end length utilized from SFM image. Experiments were done on several kinds of chains with various number and length of sections. Under the presence of divalent ions, p is about 1.3nm for short dT_{N_0}[63].

There is some consideration for the difference caused by DNA sequence[76,77]. Since the strand being comprised entirely of thymines has minimal stacking interactions[63], a series of whole adenine may give higher persistence length. It was confirmed by WLC simulation and the experiment done the similar DNA's given in figure 3.5[76]. p and monomer length b_0 of dT_{N_0} are 2~3nm and 0.5~0.7nm, respectively. In case of dA_{N_0}, however, they are 7.8nm and 0.32nm at 4°C. It seems that poly-adenines are more closely stacked (low b_0) due to strong interaction between bases, thus high persistence length is induced. More generally, the information on stacking free energy for different combinations of bases can be found in literature[78]. We may infer that the additional rigidity of dA_{N_0} is mostly enthalpic, rather than entropic. Another thing to note is that if only one different kind of base is introduced in the homogenous short chain, the stiffness is significantly reduced[77] by making a kink on the position. Some authors argue that the traditional model of DNA structure must be revised to include these sequence dependent rigidity of single-stranded DNA[77].

3.2.5 Application to the temperature probing experiment

Our polymer consists of an Au particle, a single-stranded offset, and a double-stranded part. Figure 3.8 shows how we can model this system to use equation 3.25. L_1 is the same as particle's radius and the persistence length of the section is infinite. The joint angle between section 1 and 2 ($= \beta_1$) is more or less vague. We may use chemical bond angle between gold and sulfur at the joint, but also we can think that the ssDNA is perpendicular to the gold surface($\beta_1 = 0$) due to ligand and MCH layer on the surface. β_2 is zero if smooth chain is assumed. R_1 denotes the average length from particle center to the end of ssDNA and R_2 is from the particle center to the end of dsDNA.

52

$$p_n\left(1-e^{-\frac{L_n}{p_n}}\right) \approx L_n \quad \text{as} \quad p_n \to \infty \tag{3.28}$$

Finally we can simplify equation 3.25 for R_1 and R_2.

$$R_1 = \sqrt{2}\left\{\frac{1}{2}L_1^2 + p_2^2\left[\frac{L_2}{p_2}-\left(1-e^{-\frac{L_2}{p_2}}\right)\right]+L_1p_2\left(1-e^{-\frac{L_2}{p_2}}\right)\right\}^{\frac{1}{2}} \tag{3.29}$$

$$R_2 = \sqrt{2}\left\{\frac{1}{2}L_1^2 + p_2^2\left[\frac{L_2}{p_2}-\left(1-e^{-\frac{L_2}{p_2}}\right)\right]+p_3^2\left[\frac{L_3}{p_3}-\left(1-e^{-\frac{L_3}{p_3}}\right)\right]\right.$$

$$\left.+L_1p_2\left(1-e^{-\frac{L_2}{p_2}}\right)+p_2p_3\left(1-e^{-\frac{L_2}{p_2}}\right)\left(1-e^{-\frac{L_3}{p_3}}\right)+L_1p_3\left(e^{-\frac{L_2}{p_2}}\right)\left(1-e^{-\frac{L_3}{p_3}}\right)\right\}^{\frac{1}{2}} \tag{3.30}$$

	Section 1 (gold)	Section 2 (ssDNA)	Section 3 (dsDNA)
b_0	5nm	0.63nm	0.34nm
N_0	1	25	15
$L = N_0 \cdot b_0$	5nm	15.75nm	5.1nm
p	∞	2nm	50nm
R_1	10.0nm		
R_2	12.0nm		

Table 3.2 End-to-end length of Au-ssDNA-dsDNA chain. 10nm Au particle, 25mer poly-T, and 15mer dsDNA are considered.

From the table 3.2, dsDNA of the Au-DNA conjugate is supposed to be away from the particle center by 10nm~12nm. Though overall chain length is above 20nm, the position actually we measure the temperature is just a half of it.

We probably need to compare the time scale of dehybridization and that of thermal fluctuation of DNA conformation. If the fluctuation is fast enough, then the position where
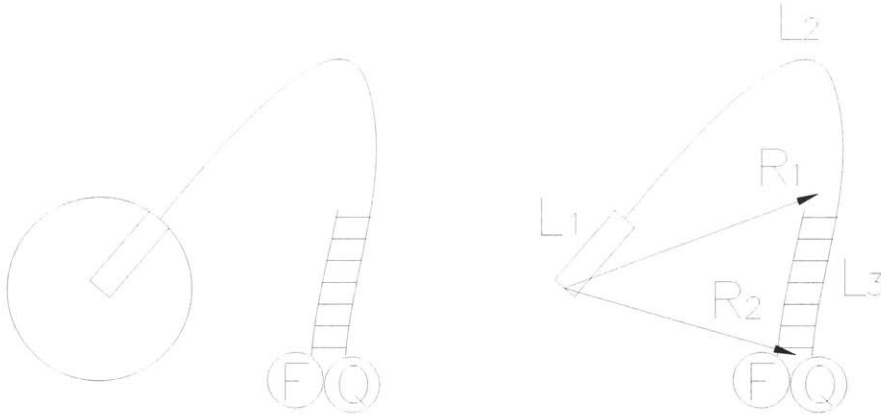
Figure 3.8 Equivalent polymer chain of Au-ssDNA-dsDNA series.

Since short dsDNA is nearly straight due to its long persistence length, we can think that the dsDNA section, which is the actual temperature probe, exists between R_1 and R_2 in average. The weakness of the modeling is that the gold particle really excludes a lot of volume. It will change the actual conformation of the DNA. If the size of the gold is not very big compared to the chain length of DNA, however, the model may give a close answer.

Table 3.2 gives an example. The offset strand is a homogeneous 25mer poly-T with the assumption of $p_1 = 2nm$, dsDNA is 15mer, and β_1, β_2 are zero. To deal with the infinite persistence length, we need to use the below relation.

$$1 - e^{-\frac{L_n}{p_n}} = 1 - \left\{ 1 - \frac{L_n}{p_n} + \frac{1}{2}\left(\frac{L_n}{p_n}\right)^2 - \cdots \right\} \approx \frac{L_n}{p_n} - \frac{1}{2}\left(\frac{L_n}{p_n}\right)^2 \quad \text{as } p_n \to \infty \qquad (3.26)$$

This leads to the following two equations.

$$p_n^2 \left[\frac{L_n}{p_n} - \left(1 - e^{-\frac{L_n}{p_n}} \right) \right] \approx \frac{1}{2} L_n^2 \quad \text{as } p_n \to \infty \qquad (3.27)$$

dehybridization occur is determined by average end-to-end length. Otherwise we have to get time distribution that end-to-end length becomes firstly smaller than a certain heating radius. This is acceptable only when the time scale of dehybridization is much smaller than that of hybridization.

At high temperature the end-to-end length becomes smaller due to decrease of persistence length. Though we considered each persistence length constant in the example, actual temperature profile may cause irregular persistence length distribution.

3.3 Nomenclatures for chapter 3

b	Kuhn length
b_0	Monomer length
c	Ion concentration [mol / l]
D_s	Self diffusivity [m^2 / s]
d	Polymer diameter
E	FRET efficiency
E_0	Electric field strength [V / m]
F	Force
K	Polymer's enthalpic spring constant
K_B	Bending stiffness
k_B	Boltzmann constant
L	Polymer chain length
l_B	Bjerrum length
N	The number of Kuhn segments ($= L / b$)
N_0	The number of monomers ($= L / b_0$)
p	Persistence length
p_0	Intrinsic persistence length / Enthalpic persistence length
p_e	Electrostatic persistence length / Entropic persistence length
p_s	Static persistence length
p_d	Dynamic persistence length
R	Root-mean-square end-to-end length of polymer

R_g	Radius of gyration
R_h	Hydrodynamic radius
R_0	Characteristic length of FRET
s	Contour coordinate
v	Velocity
Z	Partition function
z	Valency of ion
ε	Electric permittivity
η	Fluid viscosity [kg/ms]
κ^{-1}	Debye length
λ	Line charge density [Q/m]
μ_0	Electrophoretic mobility
ν	Flory exponent

Chapter 4: MCH modification of Au-DNA conjugate

In chapter 3, we saw that DNA strands conjugated to gold particles can be used as temperature probes. It was already pointed out that DNA adsorption on gold surface should be avoided to get proper information of probe's position. Thiol modified DNA's tend to make covalent bond with gold surface, but their bases also stick to the surface. Though it is known that there is some sequence and length dependent adsorption behavior, it would be advantageous to have some way to chemically destabilize nucleotide adsorption, so that constraints on sequence and length do not necessarily limit their usage.

According to previous research, 6-mercapto-1-hexanol (MCH) composes self-assembled monolayer (SAM) on flat gold surface[48]. The monolayer prevents DNA adsorption, thus enhancing the ability to hybridize with their complementary strands. This gives us an idea on how to modify our Au-DNA system to be suitable for temperature probing experiment. However, gold particles are much more difficult to deal with because they easily aggregate in liquid if they do not have enough charge to repel each other. From the experience of MCH treatment, MCH replaces not only base's adsorption sites but also displaces the charged ligand on nanoparticle surface.

Once DNA bases are detached from particle surfaces, the overall size of gold-DNA conjugates become larger. This causes mobility difference during gel electrophoresis. A theory developed to get the actual hydrodynamic size and charge of particle from the mobility change is Ferguson plot method. A review on Ferguson plot is given in chapter 4.1. Furthermore, the method is extensively used in this paper to analyze MCH treated Au-DNA conjugates. This leads to chapter 4.2, which shows how we can use MCH for particles rather than flat surface, with overcoming the aggregation problem mentioned above.

4.1 Ferguson plot and gel electrophoresis
4.1.1 Theories of Ferguson plot

The behavior of molecules in gel electrophoresis can be predicted by some models for random meshwork or cylindrical hollow pore[71,79,80]. Due to some researchers' early work, the below relationship had been established[80].

$$\frac{V_e - V_o}{V_T - V_o} = f = \frac{M}{M_o} \qquad\qquad (4.1)$$

f is the fraction of available volume to molecules V_e to total volume of gel V_T, and it is assumed to be the same as the ratio of mobility M to free mobility M_0. Void volume V_0 is identically subtracted from both the volumes. f is expressed in different forms, depending on the assumptions made on geometry of molecules and gel material, which are highly associated with the collision behavior between them[80]. For spherical molecules,

$$f = \exp\left(-s\overline{L}\right) \qquad\qquad \text{: 2-D gel structure} \qquad\qquad (4.2)$$

$$f = \exp\left(-lS/4\right) \qquad\qquad \text{: 1-D gel structure} \qquad\qquad (4.3)$$

$$f = \exp\left(-nV\right) \qquad\qquad \text{: 0-D gel structure} \qquad\qquad (4.4)$$

A gel with random planes is called a 2-D structure and 1-D gel denotes a fibrous structure. If the volume of each gel fiber is very small compared to the molecules running in gel, it is called a 0-D gel. s is the surface area of the planes per unit volume of 2-D gel, and $\overline{L}$ is the mean length of the molecule. For 1-D gel, l is the total length of fibers per unit volume and S is coupled surface area of molecules and fibers considering collisions between them. n and V of 0-D gel means the number of gel fibers per unit volume and coupled volume of molecules and fibers respectively. S and V are given below.

$$S = 4\pi(R+r)^2 \qquad \text{: Coupled surface area in 1-D gel} \qquad\qquad (4.5)$$

$$V = \frac{4}{3}\pi(R+r)^3 \qquad \text{: Coupled volume in 0-D gel} \qquad\qquad (4.6)$$

R is the radius of molecule and r is that of gel fiber.

Equation 4.7 shows the combined effect of gel pieces in different dimensions.

$$f = \exp\left\{-(s\overline{L} + lS + nV)\right\}$$ (4.7)

In reality, 1-D elements dominate in gel structure[71,80]. Thus equation 4.1, 4.3 and 4.5 can be combined as

$$\frac{M}{M_0} = \exp\left(-\pi(R+r)^2 l\right)$$ (4.8)

Note that l is in $[cm/ml]$ and M is in $[cm^2/V\cdot s]$. By taking logarithm,

$$\begin{aligned}
\log_{10} M &= \log_{10} M_0 - \left(\log_{10} e\right)\cdot \pi l(R+r)^2 \\
&= \log_{10} M_0 - \left(\log_{10} e\right)\cdot 100\pi L(R+r)^2 \cdot T \\
&= \log_{10} M_0 - K_R \cdot T
\end{aligned}$$ (4.9)

where T is gel percentage (%, $[g/100ml]$) and $L = l/T\,([cm/g])$ is the total length of fibers per unit mass of gel material. From equation 4.9, we can see that retardation coefficient K_R, which is given by $\left(\log_{10} e\right)\cdot 100\pi L(R+r)^2$, is the slope of linear equation between the logarithm of the mobility and gel percentage. Note that the fitting extrapolated to $T=0$ will give free mobility M_0. It depends on the charge density of the molecules. In addition, if we take a square root of the K_R,

$$\begin{aligned}
\sqrt{K_R} &= 10\sqrt{\log_{10} e}\left(\sqrt{\pi L}\cdot R + \sqrt{\pi L}\cdot r\right) \\
&= \left\{10\sqrt{(\log_{10} e)\pi L}\right\}\cdot R + \left\{10\sqrt{\log_{10} e}\cdot \sqrt{V_{fiber}}\right\}
\end{aligned}$$ (4.10)

V_{fiber} is the volume of fiber per unit mass, given as $\pi r^2 L\,([cm^3/g])$. Because this value is an intrinsic property of gel material that is constant, $\sqrt{K_R}$ is linearly fitted as a function of R. According to equation 4.10, larger particle gives bigger slope of Ferguson plot. This means that large molecules experience much more retardation in gel due to frequent collision with gel structure. Figure 4.1 shows the pictures of 0.5% and 4.5% agarose gel in 0.5xTBE with 2.75~10nm radius-sized gold particle. They clearly show the relation between slopes and size.
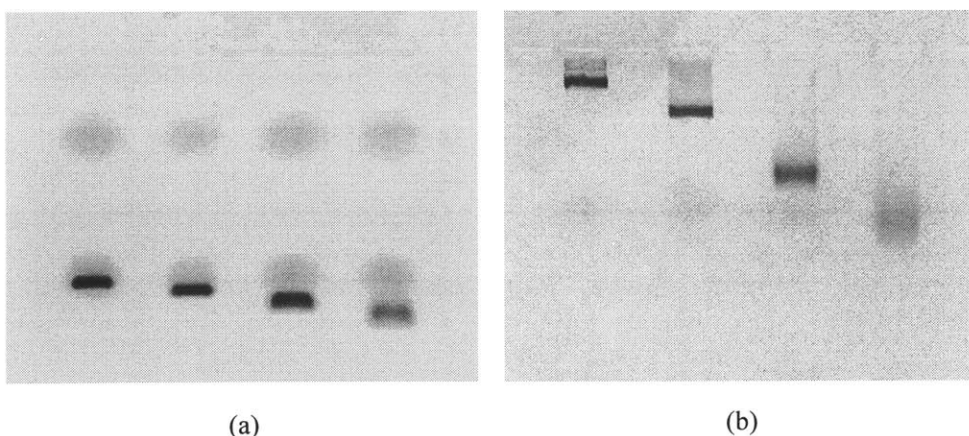
(a)   (b)

Figure 4.1 Pictures of agarose gel with Au particles. R=2.75, 4.7, 7.5 and 10nm from the left. Electric field strength is about 4V/cm. Gel percentage is (a) 0.5%, (b) 4.5%

Unfortunately, the actual fitting of $\log_{10} M$ and T is generally convex or concave depending on type of molecules. Random coiled DNA experiences reptation, which results in much less change of mobility at high gel percentage range[81-83]. On the contrary, spherical molecules experience more collisions than expected at high gel percentage, therefore the mobility rapidly decreases as T becomes high[71,81]. Figure 4.2 shows a Ferguson plot with agarose gel and ligand modified gold particles in 20nm diameter(i.e., 10nm in radius). Running buffer is 0.5xTBE.
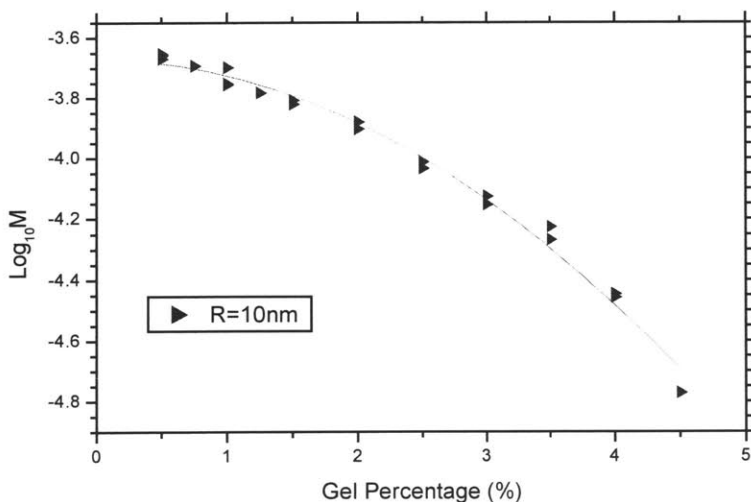

Figure 4.2 Ferguson plot with agarose gel and gold particles in 10nm radius. Gel percentage is from 0.5% to 4.5%

At low gel concentrations, the slope of the plot decreases, which means the particles hardly experience collisions below a certain level of gel concentration and shows very little change of mobility. To explain this convex behavior, a modified form of equation 4.9 was suggested[71].

$$\log_{10} M = \log_{10} M_0 - a \cdot T^b$$
$$= \log_{10} M_0 - K_R' \cdot T \tag{4.11}$$

Note $K_R' = a \cdot T^{b-1}$. In this case, $\sqrt{K_R'}$ and R is fitted to the sigmoidal function rather than linear relation.

$$\sqrt{K_R'} = \frac{(A_1 - A_2)}{1 + (R/R_0)^p} + A_2 \tag{4.12}$$

A_1, A_2, p and R_0 are determined by fitting the data. R_0 is an inflection point of the sigmoidal curve. From the experience, however, it was found that it is hard to get consistent K_R' from the fitting because it contains T^{b-1} term whose exponent is very close to zero. A significant error arises from equation 4.12, too.

To utilize equation 4.9, we need to limit the range of gel concentration[79]. For gold particles in 2.75nm ~ 10 nm radius, 1.5%~3.5% agarose gel percentage gives linear relationships by experiment (figure 4.3)
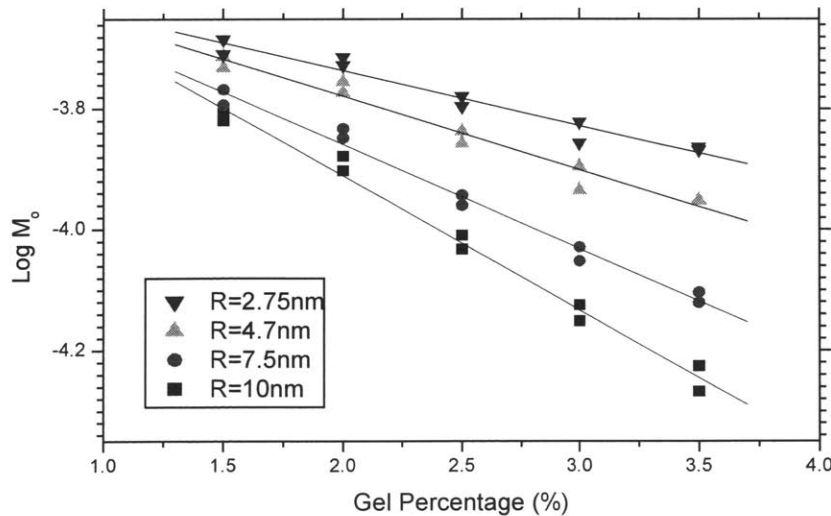

Figure 4.3 Ferguson plot with agarose gel and gold particles in 2.75~10nm radius. Gel percentage is from 1.5% to 3.5%

$\sqrt{K_R}$ can be calculated from the square root of the slopes in figure 4.3. These values are fitted again as a function of R (see equation 4.10).
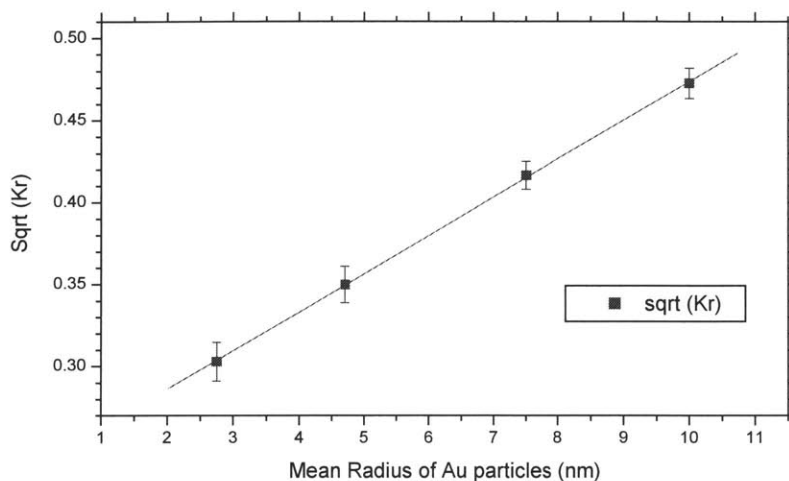

Figure 4.4 $\sqrt{K_R}$ vs. R

The fitted linear equation is given as equation 4.13 for later use.

$$\sqrt{K_R} = 0.23935 + 0.02345 \cdot R \qquad (4.13)$$

4.1.2 DNA reptation model

Gel electrophoresis is widely used for separating DNA fragments. The mobility of DNA is strongly related with its chain length. As shown in chapter 3, the polymer chain sufficiently longer than its persistence length composes globular random coil. It behaves like a spherical molecule if gel concentration is low. We probably consider radius of gyration to deal with internal viscous flow. At high gel concentration, however, the pore size may be smaller than the random coil. Under the external electric field, a part of their strand is unraveled and sneaks through the gel pores[83]. This is called reptation. To explain this phenomenon, the gel structure is treated as a porous material, rather than a matrix of fibers described in chapter 4.1.1.

Classical models of mobility in porous gel structure is given below[79,84].

$$\frac{M}{M_0} = 1 - \frac{R}{P_E} \tag{4.14}$$

$$\frac{M}{M_0} = \left(1 - \frac{R}{P_E}\right)^2 \tag{4.15}$$

$$\frac{M}{M_0} = 1 - 2.104\left(\frac{R}{P_E}\right) + 2.09\left(\frac{R}{P_E}\right)^3 - 0.95\left(\frac{R}{P_E}\right)^5 \tag{4.16}$$

$$\frac{M}{M_0} = \left(1 - \frac{R}{P_E}\right)^2 \left[1 - 2.104\left(\frac{R}{P_E}\right) + 2.09\left(\frac{R}{P_E}\right)^3 - 0.95\left(\frac{R}{P_E}\right)^5\right] \tag{4.17}$$

P_E is effective gel pore size, empirically determind by standard molecules with known size. It decreases as gel concentration becomes high. But equation 4.14~17 are still based on the assumption of spherical molecules, thus they cannot be used for reptating DNA strands.

As far as DNA strands are concerned, the size of molecule is usually given as the number of bases in the strand N_0, rather than the average end-to-end length[81-83]. For reptating DNA, the following formula known as vWBR is often used[82,83].

$$M = \frac{1}{\beta + \alpha(1 - e^{-N_0/N_c})} \tag{4.17}$$

α, β and N_c are experimentally determined. N_c is a critical number of DNA bases that is a function of gel percentage. If N_0 is replaced with zero, equation 4.17 gives $M(N_0 = 0) = 1/\beta \equiv M_s$, which means the asymptote mobility of very small DNA fragment. From the other extreme, $M(N_0 \to \infty)$ gives $1/(\beta + \alpha) \equiv M_\infty$, the mobility of infinitely long DNA chain. Equation 4.17 then can be rewritten as[82,83]

$$\frac{1}{M} = \frac{1}{M_\infty} - \left(\frac{1}{M_\infty} - \frac{1}{M_s}\right)e^{-N_0/N_c} \tag{4.18}$$

or

$$\frac{\dfrac{1}{M} - \dfrac{1}{M_\infty}}{\dfrac{1}{M_s} - \dfrac{1}{M_\infty}} = e^{-N_0/N_c}$$

(4.19)

The equation looks like equation 4.8, but N_0 is used as the size parameter instead of R.

Note that the information on gel percentage is contained in N_c.

4.2 MCH treatment on Au-DNA conjugate

4.2.1 Introduction

The molecular structure of MCH is given in figure 4.5. The structure is the same as thiol modification part of oligo except for -OH group that gives a little solubility in water. Thus MCH molecules don't screen any of bases of oligo on particle surface.
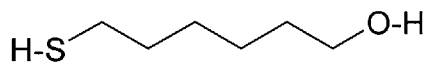

Figure 4.5 Molecular structure of 6-mercapto-1-hexanol (MCH)

Figure 4.6 shows how MCH reaction changes the conformation of Au-DNA conjugates. Oligos on gold particles are mostly adsorbed to the particle's surface before MCH being introduced. After MCH (short rod in the figure 4.6) is added to the solution, MCH molecules start replacing the adsorption sites with themselves(step 2 in the figure). Consequently, the oligo strands point outward, though still being attached to the particle by the thiol group. Further MCH reaction, however, replaces the charged ligand and oligos as well as the adsorption sites(step 3). At long times the particles lose all the ligands and oligos on the surface, and thus aggregate in the solution.

To get Au-DNA samples at step 2 or step 3 that can be used for the temperature probing experiment and future applications such as antisense, we need to stop the MCH

64

reaction at step 2 or step 3. This can be done by selective extraction of MCH with ethyl acetate. Chapter 4.2.2 will give detail description on the MCH treatment and its evaluation by use of Ferguson plot that gives actual size of the conjugates.
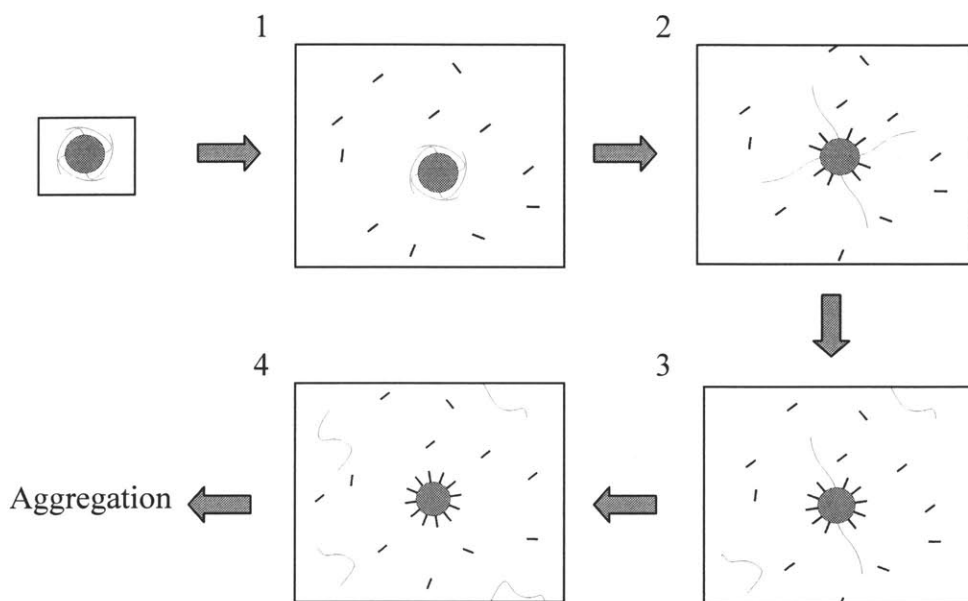

Figure 4.6 Conformation change of Au-DNA conjugate upon MCH reaction

4.2.2 Experiment

Gold nanoparticles with mean diameters 9.4nm were obtained from Ted Pella in aqueous solutions stabilized by citrate. The nanoparticle surfaces are then functionalized with bis (p-sulphonatophenyl) phenylphosphine dihydrate, dipotassium salt (BPS, Ted Pella), which has been determined to help keep the particles stable at high concentrations in aqueous solutions[85]. The BPS coated nanoparticles are precipitated from solution by addition of excess NaCl. These particles can then be resuspended into water at a higher concentration that is more amenable for visualization by gel electrophoresis. DNA oligonucleotides are purchased with C6 thiol group on the 5' end and a FAM on the 3' end (Proligo). The oligos were 15mers with a sequence 5'-HS-CCCATTGTGGATTAG-FAM-3' and purified by HPLC. Dithiol linkages between two oligos that result in oligo dimers

were initially reduced by exposure to 50mM dithiothreitol (DTT, Sigma Aldrich) for 1day prior to reaction with the gold nanoparticles. Excess DTT is removed by extraction into ethyl acetate (EM Science) at 3x the volume of the aqueous fraction multiple times (>3), which dissolves DTT but not the DNA which is charged and more hydrophilic. Conjugation is done by drying out the DNA and Au nanoparticles by lyophilization, which is found to help conjugation by increasing the collision rate between gold particles and oligos. Nanoparticle-oligo conjugates were resuspended in buffer 0.5xTBE.

The conjugates were then exposed to MCH in water, at concentrations ranging from 1μM to 1mM with reaction times 1 minute to 10 minutes. The reaction concentration of Au-DNA conjugate was 1.5×10^{-7} M. Reactions were halted by introduction of 3x volume of ethyl acetate (EtAc) three times, which extracts the excess MCH into ethyl acetate away from the DNA in H_2O. The extraction of MCH crucial as it permits control of reaction time. The samples after removal of MCH were stable as aqueous solutions at least for a month, though it is subject to the initial oligo coverage ratio. If the samples are exposed to MCH for extended periods of time, they aggregate, as the particles become neutrally charged and are no longer fully soluble in aqueous solutions due to the loss of BPS and DNA from their surface.

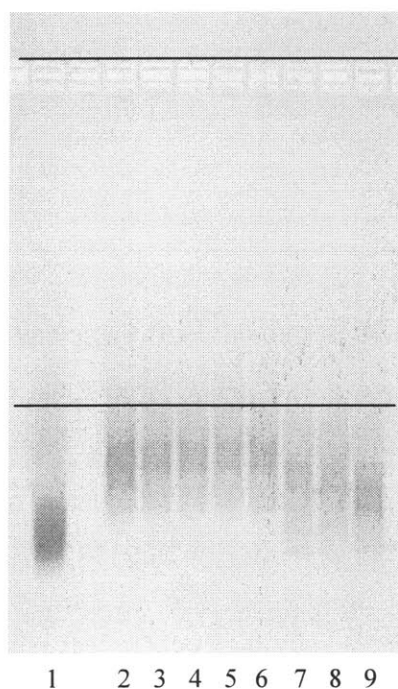

Figure 4.6 Agarose gel electrophoresis (3%) of 9.4nm Au - 15mer DNA conjugate (~1:3.7) with various MCH treatment

Lane 1: Au only
Lane 2: Au-DNA
Lane 3: Au-DNA with 1μM MCH, 1min reaction
Lane 4: 1μM, 10min
Lane 5: 10μM, 1min
Lane 6: 10μM, 10min
Lane 7: 0.1mM, 1min
Lane 8: 0.1mM, 10min
Lane 9: 1mM, 1min

In order to test the change in effective size D_H upon reaction with MCH, a
Ferguson plot method is used. Figure 4.6 shows a 3% gel containing nanoparticle-DNA
(~1:3.7 coverage ratio) samples that have been exposed to various reaction conditions. Lane
1: Au BPS alone, 2: Au-DNA, 3: Au-DNA with 1μM MCH for 1min, 4: Au-DNA with
1μM MCH for 10min, etc. 0.5xTBE was used as running buffer. The bands shift slightly
upon treatment with low concentration MCH. However, samples that have been exposed to
MCH at high concentration do not shift as much, which suggests that reaction with
concentrated MCH displaces the oligo from the nanoparticle surface and results in size
decrease.

Since the standard for particle sizing (equation 4.13) was made with 1.5~3.5% agarose gel,
the same range of gel percentage is used for the Ferguson plot of the samples. At least 4
data points are collected from each sample. Figure 4.7 shows the Ferguson plot of some Au
and Au-DNA samples.

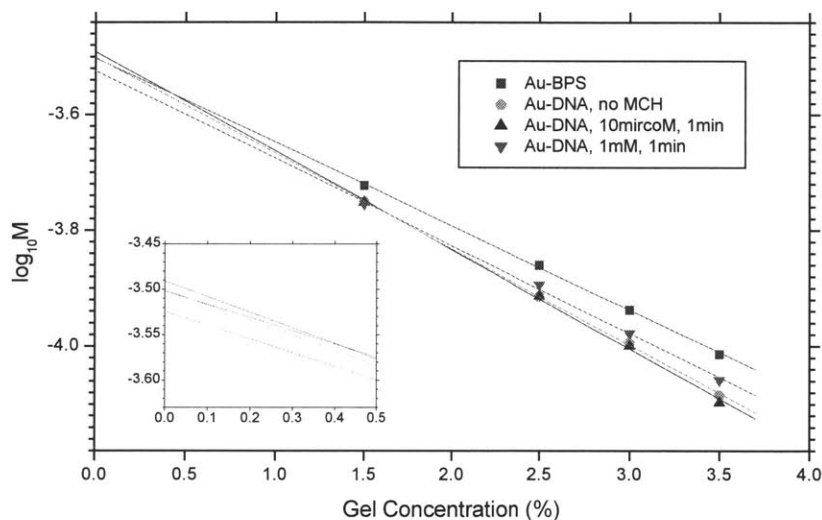
Figure 4.7 Ferguson plot of 9.4nm Au - 15mer DNA conjugate (~1:3.7) with
MCH treatment: Au(-BPS) only, Au-DNA, Au-DNA with 10μM MCH 1min, Au-
DNA with 1mM MCH, 1min. Inset : zoomed in near 0%

The figure clearly shows 1mM/1min MCH treated sample has smaller M_0 compared to the
other three samples, which means there was some charge reduction due to loss of DNA as

well as BPS. From the slope of liner fittings, we can infer the effective size D_H of each sample by use of equation 4.13.

Figure 4.8(a) shows D_H obtained from various samples. D_H is plotted as a function of the MCH concentration ($1\mu M \sim 1mM$) for a reaction time of 1 min (circles) or 10 min (squares), and is reported for coverage ratios from 1:0.4 to 1:3.7. Only the samples being stable at least for a month after MCH reaction are shown in the figure. The size differences between Au and Au-DNA without MCH treating increase as coverage ratio becomes high. Upon reaction with MCH, the size of Au-DNA with the coverage ratio above 1:1 increases by up to 0.6nm, while no noticeable change was observed from Au-DNA with the coverage ratio below 1:1. This result is consistent from multiple measurements. The change in D_H means that the oligo is changing to a lightly more radial configuration. The persistence length of single stranded DNA varies from 0.75nm to 2~3 nanometers from chapter 3, so even if the C6 linker (i.e., MCH) were perfectly packed, the 15mer oligo's actual end-to-end length is much smaller than its chain length. At MCH concentration higher than 0.1mM, D_H decreases or the particles aggregate depending on coverage ratio. This indicates that at lower concentrations the MCH initially displaces any base bonding of the oligo, but at higher concentrations MCH detaches oligo by its thiol linkage. For the longer reaction time of 10 min (squares) the increase in effective size is not very different from 1min of MCH reaction, but at higher concentrations (>0.1mM) the size decreases more than 1min reaction curve does for 1:3.7 Au-DNA, or 1:1.5 and 1:2.1 conjugates aggregate through long time according to further detachment of the oligo. This suggests that there is a certain period of time in which the MCH can disrupt the base bonding and straighten out the oligo, but after a longer period of time more MCH binds to the nanoparticle surface, competing with the thiolated oligo and eventually completely displacing the oligo. For low coverage ratio (below 1:1), there are not enough oligos on Au particles to change hydrodynamic behavior in the gel whether they are straight or not, so MCH treatment does not give any size increase. Also the Au-DNA conjugates easily aggregate by treatment of MCH at high concentrations.
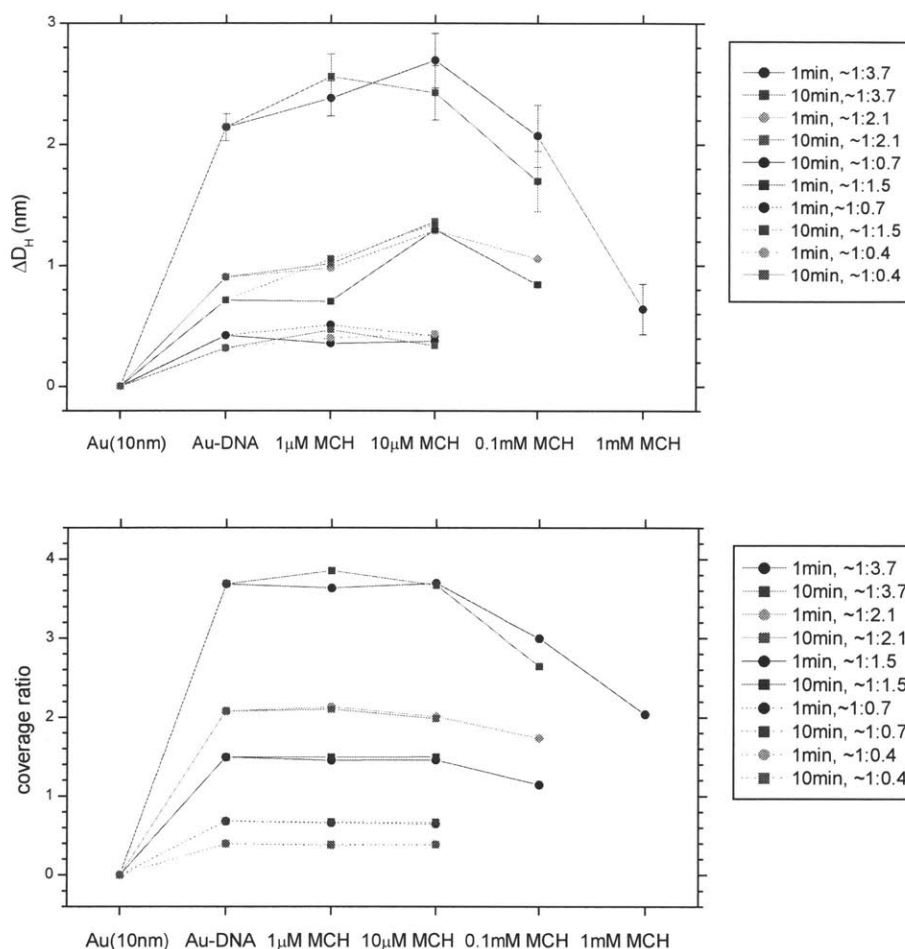
Figure 4.8 (a) 9.4nm Au - 15mer DNA conjugate's size change relative to Au
as a function of MCH reaction condition and coverage ratio and (b) their
coverage ratio

Previously, the similar molecule mercaptoethanol has been used to completely

displace the DNA oligos to allow quantification of surface coverage of the nanoparticles by

fluorescence spectroscopy[44]. Here we use MCH in excess to quantify the Au:DNA ratios by

total displacement. Samples were extracted from agarose gels thus have no free DNA.

Optical absorption at 520nm is measured to obtain the particle concentration and then the

sample is exposed to MCH at 1mM for 1 day. Completely displaced DNA was quantified

by fluorescence. The resulting surface coverage ratios are shown in Figure 4.8(b) as a

function of MCH concentration and reaction time. This plot shows that the DNA is not removed from the nanoparticle surface for the MCH concentrations at or below 10 μM observed in figure 4.8(b). However, the coverage ratio decreases at 0.1mM MCH, indicating that the DNA is displaced.

Fluorescence data was also used to show oligo displacement from the surface of the Au particles. The oligo has a FAM on the 3'end, but fluorescence is quenched by Au particles if the oligo is thiolated on the Au particle. Upon reaction with MCH, fluorescence from detached oligos can be measured, which yields kinetic data on how the MCH reaction is progressing. Fluorescence spectroscopy was performed on a Spex Fluoromax 3, with excitation at 495nm, emission collected at 517nm. Figure 4.9 shows the fluorescence intensity of 1:3.7 Au-DNA as a function of reaction times with MCH at a concentration of 0.1mM (triangles) and 10μM (circles). Samples were reacted with MCH for time varying from 1min to 10min, and washed by ethyl acetate. Then the samples were identically diluted to measure the fluorescence with reduced quenching effect from Au particles. 0.1mM MCH displaces oligo, but 10μM does not. This result is consistent with the coverage ratio changes shown in figure 4.8(b).
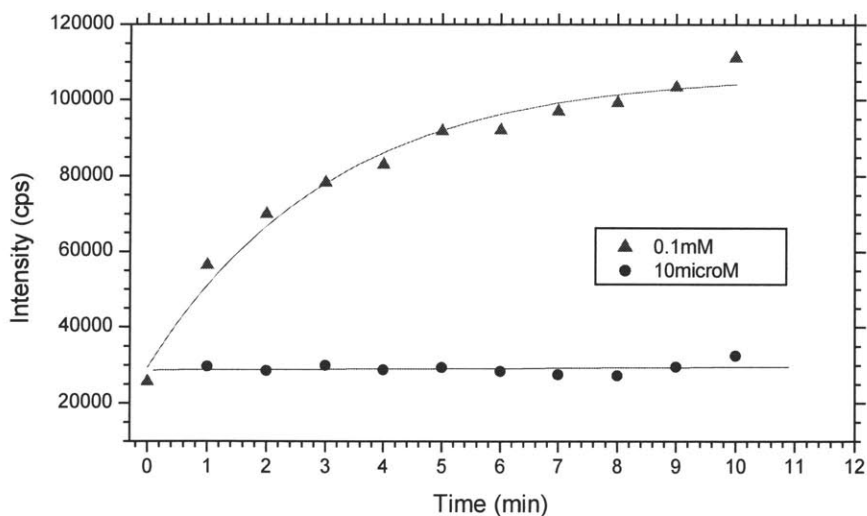

Figure 4.9 Fluorescence intensity curves as a function of MCH reaction time. Au-DNA(~1:3.7) samples were at 1×10^{-7} M during the reaction. Diluted identically for the measurement.

In summary, 9.4nm gold - 15mer DNA conjugates in 1×10^{-7} M can be modified by 1~10minutes of 10μM MCH reaction without any loss of DNA's. It is shown that this treatment effectively prevents oligo's adsorption to gold particles' surface. We can try other size of particle and oligos, or the concentration of the conjugates, but it will change the current optimized MCH concentration and reaction time since many parameters are coupled to each other. For example, bigger particle has larger surface area, thus it needs higher concentration of MCH or longer reaction time. At the same time, however, the collision rate between gold particles and MCH molecules becomes high as the particle size increases. This reduces the reaction time required.

For general usage of MCH on Au-DNA conjugates, some more different combinations of gold and oligo need to be tested. Then a trend of optimal MCH reaction condition may be achieved.

4.3 Nomenclatures for chapter 4

f Fractional volume

K_R Retardation coefficient

K_R' Modified retardation coefficient

L Fiber length per unit mass $[cm/g]$

$\bar{L}$ Mean length of molecule

l Fiber length per unit volume $[cm/ml]$

M Mobility $[cm^2/V \cdot s]$

M_0 Free mobility

M_s Mobility of infinitely short DNA

M_∞ Mobility of infinitely long DNA

N_0 The number of monomers in polymer chain

n The number of point-like gel fibers per unit volume $[1/ml]$

R Radius of molecule

r Radius of cylindrical gel fiber

S Coupled surface area of molecule and 1-D gel $(=4\pi(R+r)^2)$

s	Surface area of 2-D gel plane per unit volume $[cm^2/ml]$ or $[1/cm]$
T	Gel percentage $[g/100ml]$
V	Coupled Volume of molecule and 0-D gel $(=4/3 \cdot \pi(R+r)^3)$

5. Summary and future work

The work given in this paper was highly motivated by a previous research that showed the possibility of remote control of biomolecules through metal nanocluster antenna[1]. In alternating magnetic field metal particles are inductively heated, and the generated heat propagates to the media thus heat up biomolecules covalently linked to the particle. Since the temperature highly affects biomolecules' activity, we can control nano-scale phenomena by use of external switch.

The major heating mechanism of paramagnetic particle in classical theory is Joule loss. Alternating magnetic field induces current in the particles and this current is dissipated by internal resistance of the particle. For the nano-size system, however, we may need to adopt electron kinetics model since the physical properties of nano-system are quite different form bulk properties. From the calculation, the kinetics theory predicts less amount of power generation compared to the classical theory. Ferromagnetic particles have additional heating mechanisms. Hysterisis loss contributes only to relatively bigger particles since small ferromagnetic particles are within the regime of superparamagnetism. The super-paramagnet is mainly heated by Neel relaxation and Brownian relaxation. Due to these additional heat mechanisms, ferromagnetic particles may be preferred as an antenna in thermodynamics' sense.

Because of classical size effect, nano-size structure has low thermal conductivity in general. Phonon scatterings are mainly considered when the length scale of the system is comparable with the mean free path. According to previous research, the size effect disappears when the radius of particle is about an order bigger than phonon mean free path of medium. Since mean free path of water is very small (~0.3nm) compared to the particles mainly mentioned in this paper(~5nm), classical heat transfer equations and properties could be applied. But interface thermal resistance still exists and is not clearly explained how it affects the heat transfer. The calculated temperature profile suggested that there is not enough power to heat up gold particle and water around it. There may be unknown heating mechanisms or some problems in the power generation theory.

Because of the theories' weakness, direct temperature probing was suggested. It

may be fulfilled with a series of a particle, ssDNA and dsDNA. The segment of dsDNA has a fluorophore and a quencher on each strand. If the particle is heated, dsDNA near to particle will be dehybridized and gives unquenched fluorescence, while dsDNA outside the heating zone stays hybridized. Different lengths' of ssDNA can be used to offset dsDNA from the particle with different distances. To quantify the actual distance, worm-like chain model is used to evaluate the root-mean-square end-to-end length with the persistence length of each segment. Gold particle has infinite persistence length and that of dsDNA is about 50nm. ssDNA has much smaller persistence length varying from sub-nanometer to a few nanometers. The persistence length highly depends on salt condition that results in difference in charge screening around the DNA's backbone.

But recent research revealed that DNA bases have a tendency to stick to gold surface by donating their electron pairs. It is essential to make DNA stretched radially for the temperature probing experiment. There is some sequence dependent adsorption behavior of oligos and we may utilize it, but surface modification of gold with 6-mercapto-1-hexanol(MCH) can be a general method not depending on oligo's specific parameter. As an example, 9.4nm gold - 15mer DNA conjugates at 1×10^{-7} M were treated with various concentrations of MCH and reaction times. Their conformation changes upon MCH reaction were quantified by Ferguson plot method with agarose gel electrophoresis. It is based on the fact that larger molecules experience more rapid decrease of mobility as the gel concentration becomes high. The result shows the conjugates reacted with 10μM MCH for 1~10min have the largest effective size without any loss of DNA. At the reaction condition the DNA on the gold is believed to be stretched outward. At higher MCH concentration the conjugates lose their DNA, and further reaction results in aggregation of the particles. A combination of different sizes of particle and oligo may change the optimal reaction condition of MCH.

We are now able to assemble nano-temperature probes and possibly collect the information on temperature profile. The information is essential for controlling large and complex proteins by nanoparticle heating, where temperature gradients are expected to play a big role in the change of protein structure.

74

Whenever we develop a new antenna, we need to test its own heating behavior since the operating conditions highly depend on particle size, material, shape, magnetic field frequency and intensity, etc. If we can control different kinds of antennas with discrete magnetic field conditions, and if the antennas are conjugated to different kinds of biomolecules, then we can selectively turn on and off the molecular activities with an external control panel.

Acknowledgements

Most of all, I should thank God for being with my spirit. I cannot fully thank Hyejin for a lot of love, care and sacrifice. Also my parents and brothers should be thanked for their endless love and support.

I would like to thank Professor Kimberly Hamad-Schifferli who is the nicest and the most supportive advisor in MIT (probably in the world, too). She has given me innumerable breakthrough-advice on the research. I also thank my smart lab colleagues: Katherine Brown, Andy Wijaya, Aaron Santos, Marie-eve Aubin, Shahriar Khushrushahi and UROP students Jessica Eisenstein, Maria Tanner and Tushiyyah Lui. Their diverse backgrounds helped me extend my understanding beyond my major.

References

1. Hamad-Schifferli, K., Schwartz, J. J., Santos, A. T., Zhang, S. & Jacobson, J. M. Remote electronic control of DNA hybridization through inductive coupling to an attachd metal nanocrystal antenna. *Nature* **415**, 152-155 (2002).

2. Niemeyer, C. M. Nanoparticles, Proteins, and Nucleic Acids: Biotechnology Meets Materials Science. *Angew. Chem., Int. Ed. Engl.* **40**, 4128-4158 (2001).

3. Loweth, C. J., Caldwell, W. B., Peng, X., Alivisatos, A. P. & Schultz, P. G. DNA-Based Assembly of Gold Nanocrystals. *Angew. Chem., Int. Ed. Engl.* **38**, 1808-1812 (1999).

4. Xiao, S. et al. Selfassembly of metallic nanoparticle arrays by DNA scaffolding. *Journal of Nanoparticle Research* **4**, 313-317 (2002).

5. Hergt, R. et al. Physical limits of hyperthermia using magnetite fine particles. *IEEE Trans. Magn.* **34**, 3745-3754 (1998).

6. Thompson, M. T. Simple Models and Measurements of Magnetically Induced Heating Effects in Ferromagnetic Fluids. *IEEE Trans. Magn.* **34**, 3755-3764 (1998).

7. Rabin, Y. Is intracellualr hyperthermia superior to extracellular hyperthermia in the thermal sense? *Int. J. Hyperthermia* **18**, 194-202 (2002).

8. Hecht, E. *Optics* (Addison-Wesley, Reading, Massachusetts, 2002).

9. Zavitaev, E. V., Yushkanov, A. A. & Yalamov, Y. I. Absorption of Electromagnetic Radiation by a Cylindrical Metal Particle. *Tech. Phys.* **46**, 1460-1464 (2001).

10. Chen, G. *Nanoscale Energy Transport and Conversion : A parallel treatment of Electrons, molecules, phonons, and photons (in press)*

11. Kittel, C. *Introduction to solid state physics* (John Wiley & Sons, New York, 1996).

12. Chan, D. C. F., Kirpotin, D. B. & Jr., P. A. B. Synthesis and evaluation of colloidal magnetic iron oxides for the site specific radiofrequency-induced hyperthermia of cancer. *Int. J. Hyperthermia* **122**, 374-378 (1993).

13. Jordan, A. et al. Inductive heating of ferromagnetic particles and magnetic fluids: physical evaluation of their potential for hyperthermia. *Int. J. Hyperthermia* **9**, (1993).

14. Neel, L. Influence of thermal fluctuations on the magnetization of ferromagnetic small particles. *C. R. Acad. Sci.* **228**, 664-668 (1949).

15. Popplewell, J., Rosensweig, R. E. & Johnston, R. J. Magnetic field induced rotations in ferrofluids. *IEEE Trans. Magn.* **26**, 1852-1854 (1990).

16. Mills, A. F. *Heat Transfer* (Prentice Hall, Upper Saddle River, NJ, 1999).

17.   Incropera, F. P. & DeWitt, D. P. *Introduction to heat transfer* (John Wiley & Sons, Singapore, 1990).

18.   White, F. M. *Fluid Mechanics* (McGraw-Hill, Singapore, 1994).

19.   Flik, M. I. & Tien, C. L. *J. Heat Transfer* **112**, 872- (1990).

20.   Majumdar, A. Microsclae Heat Conduction in Dielectric Thin Films. *J. Heat Transfer* **115**, 7-16 (1993).

21.   Joshi, A. A. & Majumdar, A. Transient ballistic and diffusive phonon heat transport in thin films. *J. Appl. Phys.* **74**, 31-39 (1993).

22.   Goodson, K. E. & Flik, M. I. Electron and Phonon Thermal Conduction in Epitaxial High-T_c Superconducting Films. *J. Heat Transfer* **115**, 17-25 (1993).

23.   Joseph, D. D. & Preziosi, L. *Review Modern Physics* **61**, 41- (1989).

24.   Chen, G. Nonlocal and Nonequilibrium Heat Conduction in the Vicinity of Nanoparticles. *J. Heat Transfer* **118**, 539-545 (1996).

25.   Cahill, D. G., Goodson, K. & Majumdar, A. Thermometry and Thermal Transport in Micro/Nanoscale Solid-State Devices and StructureBiophysical Journals. *J. Heat Transfer* **124**, 223-241 (2002).

26.   Wang, X., Xu, X. & Choi, S. U. S. Thermal conductivity of Nanoparticle-Fluid Mixture. *J. Thermophys. Heat Transfer* **13**, 474-480 (1999).

27.   Keblinski, P., Phillpot, S. R., Choi, S. U. S. & Eastman, J. A. Mechanisms of heat flow in suspension of nano-sized particles (nanofluids). *Int. J. Heat Mass Transfer* **45**, 855-863 (2002).

28.   Xuan, Y. & Roetzel, W. Conceptions for heat transfer correlation of nanofluids. *Int. J. Heat Mass Transfer* **43**, 3701-3707 (2000).

29.   Xie, H., Lee, H., Youn, W. & Choi, M. Nanofluids containing multiwalled carbon nanotubes and their enhanced thermal conductivities. *J. Appl. Phys.* **94**, 4967-4971 (2003).

30.   Xie, H., Wang, J., Xi, T. & Liu, Y. Thermal Conductivity of Suspensions Containing Nanosized SiC Particles. *Int. J. Thermophys.* **23**, 571-580 (2002).

31.   Das, S. K., Putra, N., Thiesen, P. & Roetzel, W. Temperature Dependence of Thermal Conductivity Enhancement for Nanofluids. *J. Heat Transfer* **125**, 567-574 (2003).

32.   Das, S. K., Putra, N. & Roetzel, W. Pool boiling characteristics of nano-fluids. *Int. J. Heat Mass Transfer* **46**, 851-862 (2003).

33.   Xue, Q.-Z. Model for effective thermal conductivity of nanofluids. *Phys. Lett. A* **307**, 313-

317 (2003).

34. Swartz, E. T. & Pohl, R. O. Thermal Boundary Resistance. *Review Modern Physics* **61**, 605-668 (1989).

35. Stoner, R. J. & Maris, H. J. Kapitza Conductance and Heat Flow Between Solids at Temperatures From 50 to 300K. *Phys. Rev. B* **59**, 16373-16387 (1993).

36. Yu, C.-J., Richter, A. G., Datta, A., Durbin, M. K. & Dutta, P. Observation of Molecular Layering in Thin Liquid Films Using X-Ray Reflectivity. *Phys. Rev. Lett.* **82**, 2326-2329 (1999).

37. Yu, C.-J., Richter, A. G., Datta, A., Durbin, M. K. & Dutta, P. Molecular layering in a liquid on a solid substrate: an X-ray reflectivity study. *Physica B* **283**, 27-31 (2000).

38. Mulder, F. M., Stegink, T. A., Thiel, R. C., Jongh, L. J. d. & Schmid, G. Metallic behaviour in a Pt_{309} cluster revealed by ^{197}Au Mossbauer spectroscopy. *Nature* **367**, 716-718 (1994).

39. Heer, W. A. d. The physics of simple metal clusters: experimental aspects and simple models. *Rev. Mod. Phys.* **65**, 611-676 (1993).

40. Goldenberg, H. & Tranter, C. J. Heat flow in an infinite medium heated by sphere. *Brit. J. Appl. Phys.* **3**, 296-298 (1952).

41. Andra, W., d'Ambly, C. G., Hergt, R., Hilger, I. & Kaiser, W. A. Temperature distribution as function of time around a small spherical heat source of local magnetic hyperthermia. *J. Magn. Magn. Mat.* **194**, 197-203 (1999).

42. Amersham Bioscience. Fluorescence = An overview. http://www5.amershambiosciences.com/aptrix/upp00919.nsf/4a0f132842ea4d354a25685d 0011fa04/725d8c764fb246ff80256b3e00322806/$FILE/Fluorescence.pdf

43. Proligo. Reporters & Quenchers available for bi-labeled fluorescent probes. http://www.proligo.com/87256AA200670AC9/CurrentBaseLink/N25FTUWQ458AMOE EN

44. Demers, L. M. et al. A Fluorescence-Based Method for Determining the Surface Coverage and Hybridization Efficiency of Thiol-Capped Oligonucleotides Bound to Gold Thin Films and Nanoparticles. *Anal. Chem.* **72**, 5535-5541 (2000).

45. Dubertret, B., Calame, M. & Libchaber, A. J. Single-mismatch detection using gold-quenched fluorescent oligonucleotides. *Nat. Biotechnol.* **19**, 365-370 (2001).

46. Storhoff, J. J., Elghanian, R., Mirkin, C. A. & Letsinger, R. L. Sequence-Dependent Stability of DNA-Modified Gold Nanoparticles. *Langmuir* **18**, 6666-6670 (2002).

47. Parak, W. J. et al. Conformation of Oligonucleotides Attached to Gold Nanocrystals Probed by Gel Electrophoresis. *Nano Lett.* **3**, 33-36 (2003).

48. Herne, T. M. & Tarlov, M. J. Characterization of DNA Probes Immobilized on Gold Surfaces. *J. Am. Chem. Soc.* **119**, 8916 - 8920 (1997).

49. Purves, W. K., Sadava, D., Orians, G. H. & Heller, H. C. *Life: The Science of Biology* (Sinauer Associates, Sunderland, MA, 2001).

50. Bednar, J. et al. Determination of DNA Persistence Length by Cryo-electron Microscopy. Separation of the Static and Dynamic Contributions to the Apparent Persistence Length of DNA. *J. Mol. Biol.* **254**, 579-594 (1995).

51. Beaucage, G., Rane, S. & Sukumaran, S. Persistence length of Isotactic Poly(hydroxy butyrate). *Macromolecules* **30**, 4158-4162 (1997).

52. Eisenberg, E. & Baram, A. The persistence length of two-dimensional self-avoiding random walks. *J. Phys. A: Math. Gen.* **36**, L121-L124 (2003).

53. Maier, B., Bensimon, D. & Croquette, V. Replication by a Single DNA Polymerase of a Stretched Single-Stranded DNA. *Proc. Natl. Acad. Sci. USA* **97**, 12002-12007 (2000).

54. Smith, S. B., Cui, Y. & Bustamante, C. Overstretching B-DNA: The Elastic Response of Individual Double-Stranded and Single-Stranded DNA Molecules. *Science* **271**, 795-799 (1996).

55. Wang, M. D., Yin, H., Landick, R., Gelles, J. & Block, S. M. Stretching DNA with optical tweezers. *Biophys. J.* **72**, 1335-1346 (1997).

56. Smith, S. B. & Bendich, A. J. Electrophoretic charge density and persistence length of DNA as measured by fluorescence microscopy. *Biopolymers* **29**, 1167-1173 (1990).

57. Tinland, B., Pluen, A., Sturm, J. & Weill, G. Persistence Length of Single-Stranded DNA. *Macromolecules* **30**, 5763 - 5765 (1997).

58. Viovy, J.-L. Electrophoresis of DNA and other polyelectrolytes: Physical mechanisms. *Rev. Mod. Phys.* **72**, 813-872 (2000).

59. Ariel, G. & Andelman, D. Persistence length of a strongly charged rodlike polyelectrolyte in the presense of salt. *Phys. Rev. E* **67**, 011805(11) (2003).

60. Marko, J. F. & Siggia, E. D. Stretching DNA. *Macromolecules* **28**, 8759-8770 (1995).

61. Skolnick, J. & Fixman, M. Electrostatic Persistence Length of a Wormlike Polyelectrolyte. *Macromolecules* **10**, 944-948 (1977).

62. Schellman, J. A. & Harvey, S. C. Static contributions to the persistence length of DNA and dynamic contributions to DNA curvature. *Biophys. Chem.* **55**, 95-114 (1995).

63.   Rivetti, C., Walker, C. & Bustamante, C. Polymer chain statistics and conformational analysis of DNA molecules with bends or sections of different flexibility. *J. Mol. Biol.* **280**, 41-59 (1998).

64.   Murphy, M. C., Rasnik, I., Cheng, W., Lohman, T. M. & Ha, T. Probing single-stranded DNA conformational flexibility using fluorescence spectroscopy. *Biophys. J.* **86**, 2530-2537 (2004).

65.   Flory, P. J. *Statistical Mechanisms of Chain Molecules* (Interscience, New York, 1969).

66.   Smith, D. E., Perkins, T. T. & Chu, S. Dynamical Scaling of DNA Diffusion Coefficients. *Macromolecules* **29**, 1372-1373 (1996).

67.   Bouchiat, C. et al. Estimating the persistence length of a worm-like chain molecule from force extension measurements. *Biophys. J.* **76**, 409-413 (1999).

68.   Long, D., Viovy, J.-L. & Ajdari, A. Simultaneous action of electric fields and nonelectric forces on a polyelectrolyte: Motion and deformation. *Phys. Rev. Lett.* **76**, 3858-3861 (1996).

69.   Stigter, D. & Bustamante, C. Theory for the Hydrodynamic and Electrophoretic Stretch of Tethered B-DNA. *Biophys. J.* **75**, 1197–1210 (1998).

70.   Debye, P. The Intrinsic Viscosity of Polymer Solutions. *J. Chem. Phys.* **14**, 636-639 (1946).

71.   Tietz, D. & Chrambach, A. Analysis of convex Ferguson plots in agarose gel electrophoresis by empirical computer modeling. *Electrophoresis* **7**, 241-250 (1986).

72.   Perkins, T. T., Smith, D. E., Larson, R. G. & Chu, S. Stretching of a Single Tethered Polymer in a Uniform Flow. *Science* **268**, 83-87 (1995).

73.   Wang, W., Lin, J. & Schwartz, D. C. Scanning Force Microscopy of DNA Molecules Elongated by Convective Fluid Flow in an Evaporating Droplet. *Biophys. J.* **75**, 513-520 (1998).

74.   Bensimon, D., Simon, A. J., Croquette, V. & Bensimon, A. Stretching DNA with a receding meniscus: Experiments and Models. *Phys. Rev. Lett.* **74**, 4754-4757 (1995).

75.   Deniz, A. A. et al. Single-Pair Fluorescence Resonance Energy Transfer on Freely Diffusing Molecules: Observation of Forster Distance Dependence and Subpopulations. *Proc. Natl. Acad. Sci. USA* **96**, 3670-3675 (1999).

76.   Mills, J. B., Vacano, E. & Hagerman, P. J. Flexibility of Single-Stranded DNA: Use of Gapped Duplex Helices to Determine the Persistence Lengths of Poly(dT) and Poly(dA). *J. Mol. Biol.* **285**, 245-257 (1999).

77.   Goddard, N. L., Bonnet, G., Krichevsky, O. & Libchaber, A. Sequence Dependent Rigidity of Single Stranded DNA. *Phys. Rev. Lett.* **85**, 2400-2403 (2000).

78.   Friedman, R. A. & Honig, B. A Free Energy Analysis of Nucleic Acid Base Stacking in Aqueous Solution. *Biophys. J.* **69**, 1528-1535 (1995).

79.   Griess, G. A., Moreno, E. T., Easom, R. A. & Serwer, P. The Sieving of Spheres During Agarose Gel Electrophoresis: Quantitation and Modeling. *Biopolymers* **28**, 1475-1484 (1989).

80.   Rodbard, D. & Chrambach, A. Unified Theory for Gel Electrophoresis and Gel Filtration. *Proc. Natl. Acad. Sci.* **65**, 970-977 (1970).

81.   Serwer, P. Sieving of double-stranded DNA during agarose gel electrophoresis. *Electrophoresis* **10**, 327-331 (1989).

82.   Rill, R. L., Beheshti, A. & Winkle, D. H. V. DNA electrophoresis in agarose gels: Effects of field and gel concentration on the exponential dependence of reciprocal mobility on DNA length. *Electrophoresis* **23**, 2710-2719 (2002).

83.   Slater, G. W. A theoretical study of an empirical function for the mobility of DNA fragments in sieving matrices. *Electrophoresis* **23**, 1410-1416 (2002).

84.   Deen, W. M. Hindered Transport of Large Molecules in Liquid-Filled Pores. *AIChE Journal* **33**, 1409-1425 (1987).

85.   Zanchet, D., Micheel, C. M., Parak, W. J., Gerion, D. & Alivisatos, A. P. Electrophoretic Isolation of Discrete Au Nanocrystal/DNA Conjugates. *Nano Lett.* **1**, 32-35 (2001).